

## 2

# The Offshore Environment

In this chapter the properties of wind and ocean waves will be described, focusing on issues important to the extraction of wind energy and the computation of loads from wind and waves.

The main difference between land-based and offshore wind turbines is exposure to the offshore environment. In addition to wind, an offshore wind turbine is exposed to waves and currents.

The main characteristics of wind are similar over land and over the ocean. However, there are some important differences. These are, among others, related to the sea surface. In contrast to wind over land, waves on the sea surface represent a boundary for the wind, with surface roughness depending upon wave height. Further, the temperature difference between sea and air follows a different pattern over time than the temperature difference between land and air. The consequence is that the wind field offshore differs from that on land. Thus, experience gained from land-based wind turbines has some limitations when it comes to offshore turbines.

Ocean waves represent a new environmental parameter to consider when moving wind turbines offshore. A proper description of ocean waves is thus needed to establish proper estimates of fatigue and extreme loads on structures. For floating wind turbines, wave-induced motion is also an important design consideration. How much detail is needed for the description of wave kinematics depends upon the geometry of the support structure, the load cases considered and, e.g., the relative importance of wind versus wave loads. For some applications, a linearization of the kinematics and loads is sufficient, while in other cases a careful description of the kinematics of the extreme waves should be considered.

Ocean currents in most cases do not themselves represent critical loads. However, currents modify waves and may thus modify wave-induced loads. For bottom-fixed support structures, a speed-up of currents close to the seabed may cause the transport of sediments away from the immediate vicinity of the wind

turbine foundation in a phenomenon called scouring. Scouring may deteriorate the fixture of the wind turbine to the sea floor.

In the following, some basic principles for describing the wind field and ocean waves are presented. The description of the theoretical background and the level of detail are limited. To get a deeper insight into the material presented, please see the references given.

## **2.1 Wind**

### ***2.1.1 Introduction***

For offshore wind turbines, the wind represents the energy resource. However, the wind also causes loads on the turbine structure. These loads must be accounted for in the design. In applications related to offshore wind farms, the wind field must be understood and described across a wide range of length and timescales. In the design of rotor blades, the turbulent structures of the wind field in the range of meters and seconds are important in the assessment of dynamic loads, while to understand the flow inside and in the vicinity of a wind farm length scales in the range of hundreds of meters to several kilometers and time scales in the range of a few minutes to hours must be considered. Prediction of the energy production hours ahead requires an understanding of the wind field at meso-scale range (tens of kilometers in length and hours in time).

In the design of offshore structures, simplistic descriptions of the wind field have been used in most cases. This is because the focus has been on the estimation of extreme loads with probability of occurrence in the range  $10^{-2}$ – $10^{-4}$  per year. For offshore wind turbines the needs are different. Still, extreme as well as operational loads are important factors in design. However, as the largest rotors exceed 200 m in diameter and are very slender and flexible structures, a detailed understanding of the structure of the wind field is very important, from both a power extraction and a structural design point of view.

A thorough description of the turbulent wind field over the ocean will not be given here. For a detailed description of the meteorology of the atmospheric boundary layer, reference is made to special textbooks, e.g., Lee (2018) and Stull (1988). The following description will restrict the discussion to some of the main parameters used to describe the wind field suitable for the design of wind turbines. It will also address some of the challenges encountered, such as with increased rotor sizes. Relevant time and length scales are illustrated in Figure 2.1.

### ***2.1.2 The Marine Atmospheric Boundary Layer***

The atmospheric boundary layer<sup>1</sup> is the region between ground or sea surface and the “free” atmosphere. In the free atmosphere the effect of the surface friction on

<sup>1</sup> The general discussion of the atmospheric boundary layer is valid for boundary layers both over sea and land. When the marine atmospheric boundary layer is considered, the abbreviation MABL is used.

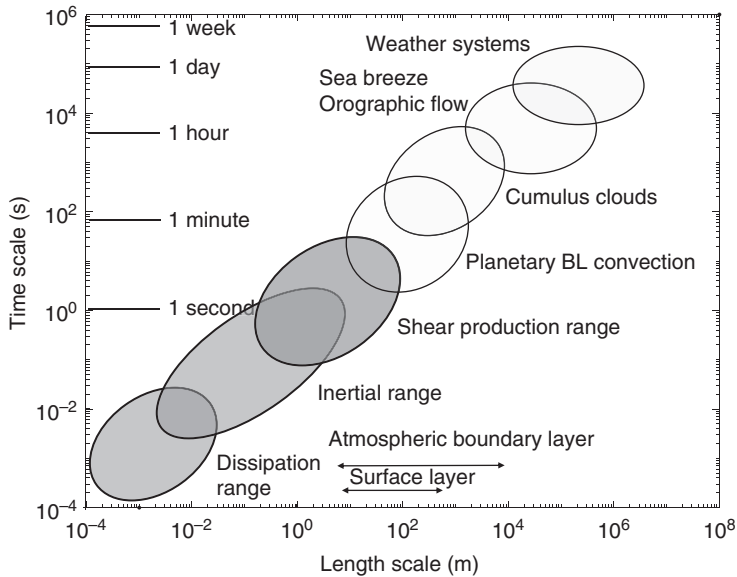


Figure 2.1 Illustration of the various time and length scales involved in the atmospheric flow. The three ranges considered for wind turbines are marked in bold. Based upon an original figure in Busch et al. (1978). Reproduced with permission of Springer eBook.

the wind field can be ignored. Between the free atmosphere and the boundary layer there frequently exists a capping layer, which limits the exchange of air between the boundary layer and the free atmosphere. The elevation of this capping or inversion layer is highly dependent upon the weather conditions. The various layers of the atmospheric boundary layer are illustrated in Figure 2.2. A typical order of magnitude of the elevation of the capping layer during neutral and unstable atmospheric conditions, also denoted as convective conditions, may be around 1 km. However, this may vary a lot and during stable atmospheric conditions the elevation of the capping layer can be as low as a few hundred meters and even below 100 m. Atmospheric stability is discussed in more detail in Section 2.1.2.2. In the upper part of the boundary layer, also denoted as the Ekman layer, the direction of the mean wind is strongly influenced by the combined effect of the Coriolis forces and the vertical gradient of the mean wind speed, causing a continuous shift of mean wind direction down through the boundary layer. The lower part of the boundary layer is called the surface layer. The thickness of the surface layer is in the order of 10% of the boundary layer, and traditionally it has been assumed that wind turbines operate in this layer. However, large offshore wind turbines may operate above this height. In the surface layer the turbulent mixing due to vertical velocity shear is

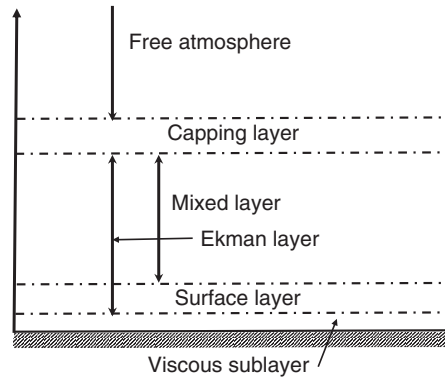


Figure 2.2 Various parts of the atmospheric boundary layer. Not to scale. The mixed layer is also denoted as the convective layer.

significant, but also temperature (buoyancy) effects may be important for the turbulence. In the immediate vicinity of the ground or sea, there is a viscous sublayer. We will focus here on the surface layer. The considerations are somewhat simplified as, e.g., the Coriolis forces are neglected, as is frequently done in wind energy applications.

### 2.1.2.1 Mean Velocity Profile

To describe the flow field in the atmospheric boundary layer, the Navier–Stokes equations are invoked. In Appendix A, a brief summary of the two-dimensional boundary layer equations for an incompressible flow is given. Here, some classical relations between the mean velocity profile, the fluctuating velocity components and the shear are given. These relations are utilized in describing some key characteristics for the MABL.

A Cartesian coordinate system is used, with the  $x$ -axis horizontal and positive in the mean wind direction and the  $z$ -axis vertical, positive upwards and zero at the sea level. The velocity in  $x$ -direction can then be written as a mean value plus the turbulent fluctuation,  $u = \bar{u} + u'$ . The mean transverse and vertical velocities are assumed to be zero, while the fluctuating components are denoted as  $v'$  and  $w'$  respectively. The variation in mean wind direction with height due to the Coriolis effect is thus disregarded. In solving the Navier–Stokes equations for the mean flow, a closure problem exists. Terms denoted Reynolds stresses of the form  $\rho_a \overline{u'w'}$ ,  $\rho_a \overline{u'v'}$  and  $\rho_a \overline{v'w'}$  appear in the equations, where  $\rho_a$  is the density of air. The Reynolds stresses are related to characteristics of the mean flow. Based upon empirical evidence, the Reynolds stresses are assumed proportional to the vertical velocity gradient in the boundary layer. This is according to the Prandtl mixing

length theory; see, for example, Curle and Davies (1968). In a two-dimensional flow, the Reynolds stress is written as:

$$\rho_a \overline{u'w'} = -K_m \rho_a \frac{\partial \bar{u}}{\partial z}. \quad [2.1]$$

$K_m$  is denoted as the eddy diffusivity. In the absence of heat fluxes, the boundary layer is denoted as neutral. Under such conditions and close to a smooth surface but above the viscous sublayer (see Appendix A),  $K_m$  may be parameterized as:

$$K_m = k_a z u_*. \quad [2.2]$$

$k_a$  is the von Kármán constant, based upon experimental data found to be approximately 0.40.  $u_*$  denotes the friction velocity and is given from the relation  $u_* = \sqrt{\tau/\rho_a}$ , where  $\tau$  is the shear stress at the surface. In the surface layer it is assumed that the turbulent momentum fluxes are constant in the vertical direction. Thus, by combining Equations 2.1 and 2.2, and integrating from the bottom of the surface layer,  $z_0$  to  $z$ , the velocity profile is obtained as:

$$\bar{u}(z) = \frac{u_*}{k_a} \ln\left(\frac{z}{z_0}\right). \quad [2.3]$$

$z_0$  is frequently denoted as the surface roughness length scale. Charnock (1955) found a relation between  $z_0$  and  $u_*$  by measuring the wind field over a water reservoir. The vertical profile of the lowest 8 m over the water surface fitted the logarithmic profile in Equation 2.3 well. The mean velocity profile in the surface layer thus gives  $\bar{u}(z_0) = 0$ , even if the mean velocity at top of the friction layer has some small but finite value. Charnock (1955) found the empiric relation between the roughness length scale and the friction velocity as:

$$z_0 = \alpha_0 \frac{u_*^2}{g}. \quad [2.4]$$

This is called the Charnock relation. Over open sea, with fully developed waves, the Charnock constant  $\alpha_0$  has, according to DNV (2021c), values in the range of 0.011–0.014, and near coastal sites it may be 0.018 or higher.

For offshore conditions,  $z_0$  and  $u_*$  depend upon the wind speed, upstream distance from land and wave conditions. DNV (2021c) proposes  $z_0$  in the range 0.0001 to 0.01 for open sea conditions. The lowest value corresponds to calm water and the highest to rough wave conditions. Onshore, higher values for  $z_0$  apply.

The friction velocity may be related to the mean velocity at a certain vertical elevation and a surface friction coefficient. Frequently, the 10 min mean wind velocity at a height  $z_r$  over the ground or sea surface, denoted  $U_{10}(z_r)$ , is used as a reference. By combining the above relations and defining a surface friction coefficient  $\kappa = \tau/\rho_a U_{10}^2(z_r)$ , the following expression for the friction velocity and friction coefficient is obtained:

$$u_* = \sqrt{\kappa} U_{10}(z_r)$$

$$\kappa = \frac{k_a^2}{\left(\ln\left(\frac{z_r}{z_0}\right)\right)^2}. \quad [2.5]$$

Frequently, a reference height  $z_r = 10\text{ m}$  is used. With the above range of  $z_0$ ,  $\kappa$ - values in the range 0.0012 and 0.0034 are obtained.

The above formulations rely upon the assumption of a near neutral boundary layer and constant turbulent momentum fluxes in the vertical direction. Above the surface layer and in stable or unstable boundary layers the assumptions are not valid. Below the surface layer, in the viscous sublayer with a vertical extent in the order of mm, the flow is mainly laminar and is, as the name indicates, dominated by viscous effects. Viscous effects do not play an important role above this layer. Some more details related to the two-dimensional boundary layer equations are outlined in Appendix A.

In engineering applications, [2.3] is frequently replaced by a simpler power function, written as:

$$U_{10}(z) = U_{10}(z_r) \left(\frac{z}{z_r}\right)^\alpha. \quad [2.6]$$

Here,  $U_{10}(z)$  is the 10 min mean wind velocity at vertical level  $z$ . By requiring the mean wind speed at the vertical level  $z$  as obtained by [2.3] and [2.6] to be equal, a relation between  $z_0$  and  $\alpha$  is obtained:

$$\alpha(z) = \frac{\ln\left(\frac{\ln(z/z_0)}{\ln(z_r/z_0)}\right)}{\ln(z/z_r)}. \quad [2.7]$$

The result is plotted in Figure 2.3 (left) for three different values of the roughness length,  $z_0$ . It is observed that the proper  $\alpha$  value depends upon at which height the two expressions for the mean velocity are required to fit. In Figure 2.3 (right), the relation between  $z_0$  and  $\alpha$  for three different fitting heights is plotted. A reference height of  $z_r = 10\text{ m}$  is applied in the graphs.

As indicated above, the mean wind velocity depends upon the time of averaging. When considering extreme wind velocities, the extreme mean velocity with a

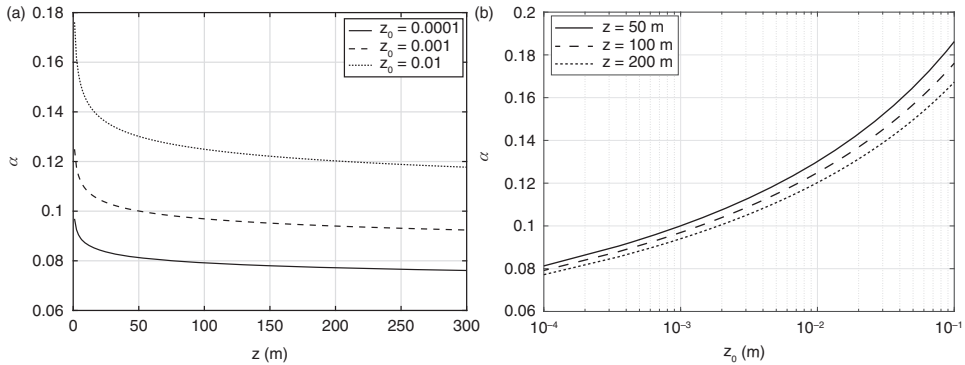


Figure 2.3 Relation between roughness length,  $z_0$  and the exponent  $\alpha$  in the power law formulation of the mean wind profile. Left: height dependence of  $\alpha$  for three different  $z_0$ . The logarithmic and exponential profile gives the same mean wind speed at height  $z$ . Right:  $\alpha$  versus  $z_0$  for three different heights. Mean wind speed fits at vertical level  $z$ . Reference height  $z_r = 10$  m is used.

certain return period, for example 10 or 50 years (corresponding to a yearly probability of occurrence of 0.1 and 0.02, respectively), increases if the time of averaging is reduced, e.g., from 1 h to 10 min. The extreme wind velocity also increases with increased turbulence intensity.

The above wind profiles should be used with care in heights above approximately 100 m as the assumption of constant turbulent fluxes above this level may be doubtful. Few wind measurements of the mean wind profile above this level exist. An example on data beyond this level is *rawinsonde* data, as discussed by Furevik and Haakenstad (2012).<sup>2</sup> Another option to measure the wind speed at high elevations is by using Lidars; see Section 2.1.5.3.

### 2.1.2.2 Stability

The mean velocity profiles discussed in the previous section are obtained assuming constant turbulent fluxes in vertical direction and neutral stability of the atmosphere. During unstable and stable atmospheric conditions, the profiles must be modified.

The atmospheric stability is related to the vertical temperature profile in the air. In simple terms, the stability condition may be understood by considering a volume of air (an air parcel) at a certain vertical level. In the initial position of the parcel, the temperature inside the parcel is equal to the temperature of the surroundings. Moving this parcel upwards causes the volume to expand due to the reduced pressure. The expansion implies work is done. Assuming the expansion is adiabatic, i.e., there is no

<sup>2</sup> A rawinsonde is a balloon equipped with instruments that is released from the ground or a ship. It measures parameters such as pressure, temperature, relative humidity and position (by GPS) on its way up to altitudes of greater than 30 km. Sometimes a rawinsonde is called a radiosonde; however, a radiosonde normally does not measure position (see the National Weather Service website, [www.weather.gov/](http://www.weather.gov/); accessed December 2022).

heat exchange with the exterior, the temperature in the parcel is reduced. If this new temperature is equal to the surrounding temperature, the density of the air in the parcel is equal to the density of the surrounding air and there is an equilibrium, or neutral stability. If, on the other hand, the temperature inside the expanded parcel is lower than the external temperature, the density of the air in the parcel is higher than the density of the surrounding air. The parcel will thus tend to sink back down to its original position, i.e., the conditions are stable. However, if the temperature of the air parcel in the new vertical position is higher than the surrounding temperature, the air parcel will tend to move further upward, i.e., the conditions are unstable.

Assuming dry air, the adiabatic expansion or compression of the air parcel will behave according to the ideal gas law:

$$\begin{aligned} pV &= nRT \\ pV^\gamma &= \text{Constant.} \end{aligned} \quad [2.8]$$

Here,  $n$  is the number of moles in the volume,  $R$  is the universal gas constant,  $V$  is the volume considered,  $p$  is the absolute pressure,  $T$  is the absolute temperature and  $\gamma = c_p/c_v$  is the gas constant for air.  $c_p$  is the specific heat under constant pressure, while  $c_v$  is the specific heat under constant volume. For dry air,  $\gamma = 1.40$ . Combining the expressions in [2.8], the temperature  $T_1$  at pressure  $p_1$  is obtained as:

$$T_1 = T_0 \left( \frac{p_0}{p_1} \right)^{\frac{1-\gamma}{\gamma}}. \quad [2.9]$$

$T_0$  and  $p_0$  define an initial state of the gas.

### Vertical Temperature Variation

*Assume the temperature at ground level is 20°C or 293 K. Normal air pressure  $p_0 = 1013$  hPa. With an air density of 1.225 kg/m<sup>3</sup>, the pressure difference at 100 m versus at ground level becomes  $\Delta p = -\rho_a g \Delta z = -1.225 * 9.80665 * 100 = -1201.3$  Pa. The temperature at 100 m elevation, assuming adiabatic expansion, becomes:*

$$T_{(z=100m)} = T_{(z=0m)} \left( \frac{p_0}{p_0 + \Delta p} \right)^{\frac{1-\gamma}{\gamma}} = 292.00 \text{ K.}$$

*I.e., under the assumption of dry air, the temperature is lowered by 1°C per 100 m of increased elevation. The requirement of “dry air” is strict; the relation holds also if no phase change takes place and there is no heat transfer by radiation. Note that the change in density with pressure has been ignored as we are considering small pressure differences.*

*If the air contains a lot of water vapour, condensation of water may take place as the air is cooled. The condensation releases heat, resulting in a lower temperature decay. The effect is temperature- and pressure-dependent, but in most cases the lapse rate is in the range of 0.5–1.0°C per 100 m.*



In studying the atmospheric boundary layer, it is convenient to use the potential temperature,  $\theta$ , rather than the sensible (measured) temperature,  $T$ . To obtain the potential temperature, assume that the air at any  $z$ - level is moved adiabatically downwards to the ground level. The temperature the air then will obtain is the potential temperature. Assuming dry air, the potential temperature becomes:

$$\theta = T_z \left( \frac{p_z}{p_0} \right)^{\frac{1-\gamma}{\gamma}} . \quad [2.10]$$

Thus, in a neutral stratified atmosphere, the potential temperature is constant with height.

Over land, the ground is heated during the day and cools at night. Over sea, the diurnal variation vanishes, as the incoming radiative energy is efficiently distributed over a large volume of water. Therefore, over the sea, the synoptic weather situation, e.g., cold air advection with northerly winds (in the northern hemisphere) over relatively warm water, or warm air advection with southerly winds over relatively cooler water, and seasonal effects control the stability of the marine atmospheric boundary layer. The first example, cold air over warm water, happens most frequently during autumn and winter and causes an unstable or convective situation, while the case of warm air over cold water occurs more frequently during spring and summer, causing a stable situation. In Figure 2.4, a simplistic illustration of the vertical profile of the potential temperature in the case of stable, neutral and unstable (convective) conditions is given. Figure 2.6 illustrates the vertical variation of the mean wind speed for the unstable, neutral and stable conditions. Here the simple exponential velocity profile, [2.6] is assumed.

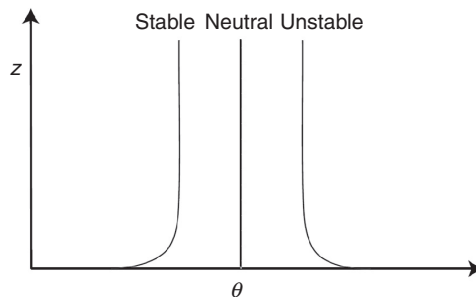


Figure 2.4 Simplistic illustration of the vertical distribution of the potential temperature in the surface layer. Stable, neutral and unstable conditions.

During unstable, or convective, conditions, the air close to the sea surface will be warmed by the sea and tend to move upwards, causing vertical mixing due to the buoyancy effect. The lower part of the boundary layer, in the region with a negative gradient of the potential temperature, the combined effect of turbulent shear stresses and buoyancy effects gives good vertical mixing. Above the surface layer, in the mixed layer, the potential temperature is almost constant. In the mixed layer, the vertical gradient of the mean velocity is low. The mixed layer may extend to about 1 km above sea level. Above the mixed layer, normally an inversion or capping layer exists, where the potential temperature increases and thus partly blocks the mixing of air into the free atmosphere. During unstable conditions, the surface layer may become fairly thick, in the order of 100–200 m. An illustration of the potential temperature through the various layers is given in Figure 2.5 (left).

During stable conditions the potential temperature increases from the sea level upwards. As the velocity gradient is large close to the sea surface, the vertical mixing is efficient in this region. Further up, however, the mixing is suppressed by the positive gradient of the potential temperature and the mixing diminishes. A vertical distribution of potential temperature through the various layers is illustrated in Figure 2.5 (right). During stable conditions, the surface layer is thinner than during unstable conditions, perhaps even less than 50 m. Above the surface layer, a residual layer is present where the potential temperature has a slightly positive gradient and the turbulent mixing is low.

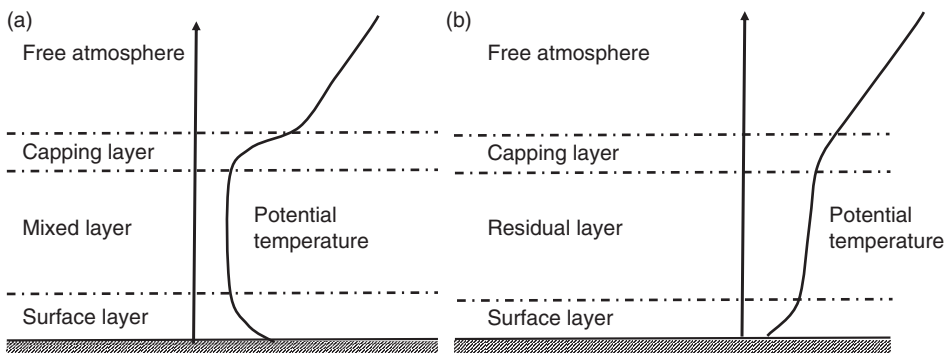


Figure 2.5 Illustration of the potential temperature variation through the various layers of the atmospheric boundary layer during unstable (convective; left) and stable (right) conditions. Based on Lee (2018). Reproduced with permission of Springer eBook.

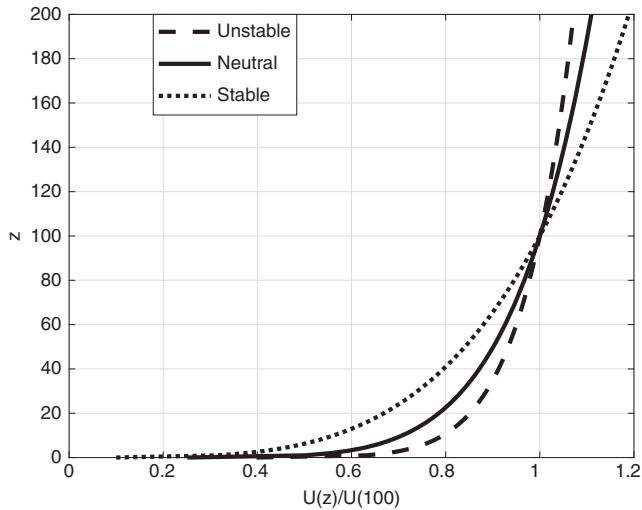


Figure 2.6 Illustration of mean wind profiles in the surface layer at different atmospheric stability conditions, assuming same mean velocity at height 100 m.

Coriolis forces act on the wind field. As the mean wind speed in general increases with height, Coriolis forces causes the wind direction to change with height. In the northern hemisphere, the wind direction at ground level is directed to the left relative to the wind direction above the boundary layer, the geostrophic wind.<sup>3</sup>

There are various ways to characterize the atmospheric stability conditions. A simple, qualitative assessment of the static stability can be performed by considering the gradient of the potential temperature.<sup>4</sup>  $\partial\bar{\theta}/\partial z < 0$  corresponds to unstable conditions,  $\partial\bar{\theta}/\partial z = 0$  corresponds to neutral conditions, while  $\partial\bar{\theta}/\partial z > 0$  corresponds to stable conditions.

A physical, consistent way to quantify the degree of stability of the boundary layer is to compare the contribution by velocity shear and buoyancy effects to the production of turbulent kinetic energy. The buoyancy effect may, depending upon the sign of the surface heat flux, both increase and decrease the kinetic turbulent energy. The flux Richardson number – see, e.g., Lee (2018) – expresses the ratio between the buoyancy and velocity shear effects in the production of turbulent kinetic energy. The flux Richardson number is written as:

<sup>3</sup> Above the boundary layer, the wind direction is determined from a balance between the pressure gradient force and the Coriolis force. The Coriolis force deflects the wind direction away from the direction of the pressure gradient (toward the right in the northern hemisphere) until the wind direction is parallel to the isobars. This is denoted as geostrophic wind.

<sup>4</sup> In the calculation of potential temperature, dry air is assumed. Frequently, the virtual potential temperature is used. In the virtual potential temperature, the humidity of the air is accounted for.

$$R = \frac{\text{buoyancy production}}{\text{shear production}} = \frac{\frac{g}{\theta} \overline{w'\theta'}}{u'w' \frac{\partial u}{\partial z}}. \quad [2.11]$$

Shear production is the shear stress times the gradient of the mean velocity.  $\theta'$  denotes the turbulent potential temperature fluctuations, similar to the velocity fluctuations. The relation is derived by using the two-dimensional Navier–Stokes equation. In deriving the relation for the buoyancy production, the vertical pressure gradient set to  $-\rho g$  and the relation between the density and the temperature is according to the ideal gas law. The minus sign in the shear production term (see Appendix A) has been omitted.  $R = 0$  corresponds to no buoyancy effects and thus a neutral condition.  $R < 0$  corresponds to positive buoyancy effects and thus an unstable condition. At  $R = -1$  the turbulence production from buoyancy effects and the velocity shear effect are equal.  $R > 0$  indicates a stable condition. Theoretically,  $R = 1$  represents an upper limit at which the destruction of turbulence caused by the buoyancy balances the production due to the vertical shear.

The flux Richardson number is height-dependent. This is not explicitly shown in [2.11]. However, as discussed above, in the surface layer, where constant vertical flux of turbulence may be assumed, the velocity gradient may be expressed by [2.3]. Further, using that  $-u'w' = u_*^2$  in the surface layer, the flux Richardson number may be written as:

$$R = \frac{\frac{g}{\theta} \overline{w'\theta'}}{-\frac{u_*^3}{k_a z}} = \frac{z}{-\frac{u_*^3}{k_a \frac{g}{\theta} \overline{w'\theta'}}} = \frac{z}{L}. \quad [2.12]$$

Here,  $L$  denotes the Obukhov length (also denoted the Monin–Obukhov length). As the Obukhov length is expressed by the surface friction and the vertical turbulent heat flux, it is independent of height (in the region of validity of the assumptions applied). It is therefore frequently used to classify the stability of the boundary layer. Van Wijk et al. (1990) propose the following ranges for characterization of stability.

Very stable:	$0 \text{ m} < L < 200 \text{ m}$
Stable:	$200 \text{ m} < L < 1000 \text{ m}$
Near neutral:	$ L  > 1000 \text{ m}$
Unstable:	$-1000 \text{ m} < L < -200 \text{ m}$
Very unstable:	$-200 \text{ m} < L < 0 \text{ m}$

A discussion of measured offshore wind speeds, turbulence and stability is found in Nybø et al. (2019) and Nybø et al. (2020). In Figure 2.7, the various regions of stability are shown as a function of the inverse of the Obukhov length.

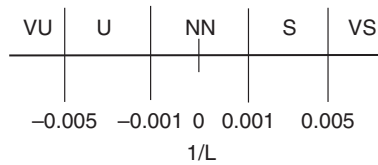


Figure 2.7 Regions of stability as a function of the inverse of the Obukhov length,  $1/L$ . VU: very unstable; U: unstable; NN: near neutral; S: stable; VS: very stable.

As the quantities used in the flux Richardson number are not readily available, an alternative is to use the gradient Richardson number. Here, the ratio between the gradient of the potential temperature and the gradient of the square of the mean wind speed is considered. The flux Richardson and gradient Richardson numbers are related via the eddy diffusivities for eddies and heat; for details, see Lee (2018).

### 2.1.2.3 Shear Exponent and Stability

Over land, the shift between stable and unstable conditions in the atmospheric boundary layer frequently follows a diurnal period. As mentioned in Section 2.1.2.2, the heat exchange between sea and atmosphere differs from that between land and atmosphere. This affects the stability condition of the atmospheric boundary layer and thus the vertical shear profile of the mean wind speed. Figure 2.8 illustrates how the shear exponent  $\alpha$  in [2.6] may vary over the year at an offshore location in the North Sea (Myren, 2021). The results are obtained by considering 11 years of hindcast data in the NORA3 dataset (Haakenstad et al., 2021). In Figure 2.8 it is also observed that the variation shear exponent closely follows the temperature difference between 100 m elevation and sea level,  $\Delta T = T_{100} - T_0$ . With this difference less than  $-1^\circ\text{C}$ , stable atmospheric conditions may be assumed. In the case shown in Figure 2.8, this happens most frequently during autumn and winter. The study by Myren (2021) showed that the variations over the year were less pronounced as the location moved farther north and farther offshore. This may be explained by lower variation between sea and air temperature in these regions.

It should be noted that the shear exponents in Figure 2.8 in general are lower than recommended in many standards. DNV (2021c) recommends a general  $\alpha$ -value over open sea with waves offshore equal to 0.12. This value does not account for atmospheric stability. However, DNV (2021c) gives advice on how the shear profile may be adjusted considering the Obukhov length. The IEC standard 64100-3 (2009) recommends the “normal wind profile” over sea  $\alpha = 0.14$ , using the reference height equal to hub height. For extreme wind speeds averaged over 3 s and a return period of 50 years, IEC 64100-3 (2009) recommends  $\alpha = 0.11$  and use of a gust factor of 1.1. No correction for stability conditions is included in this case.

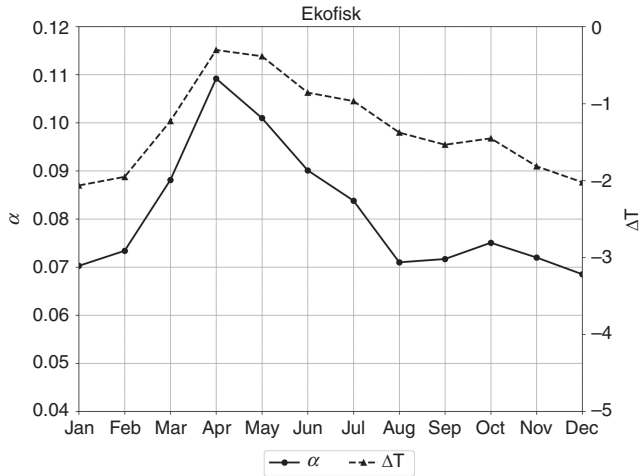


Figure 2.8 Hourly mean shear exponent,  $\alpha$ , at the Ekofisk area (left axis).  $\alpha$  obtained from NORA3 hindcast data (Haakenstad et al., 2021). The dashed line (right axis) shows the mean temperature difference between 100 m above sea level and sea surface. Time period 2004–2015. Courtesy of Myren (2021).

Furevik and Haakenstad (2012) studied a large number of offshore wind conditions where both measured and hindcast wind profiles were available. They defined the stable, near neutral and unstable conditions from the temperature difference  $\Delta T_{150}$  between the temperature 150 m above sea level and the sea temperature. The unstable, near neutral and stable conditions were defined by  $\Delta T_{150} < -1$ ,  $-1 \leq \Delta T_{150} \leq 0$ ,  $\Delta T_{150} > 0$ .  $\Delta T_{150}$  in °C. The corresponding average  $\alpha$ -values were found as 0.04, 0.05 and 0.09. These  $\alpha$ -values are, as the hindcast data above, lower than recommended by the standards. In all standard wind energy applications an increasing wind speed with height has been assumed. Furevik and Haakenstad (2012) observed frequently (in more than 1500 of 8700 cases) a decreasing wind speed with height. In general, these cases had unstable atmospheric conditions. The observations were made in the North Atlantic on the weather ship *Polarfront*.<sup>5</sup>

#### 2.1.2.4 Turbulence

As discussed above, the wind speed at a specific point may be characterized by the mean value plus a stochastic variation,  $u = \bar{u} + u'$ . The turbulence level is characterized by the standard deviation of the wind speed,  $\sigma_u = \sigma_{u'}$ . Also, the transverse and the vertical components of the velocity fluctuations are of importance. However, traditionally, and partly due to the measurements available, the wind

<sup>5</sup> *Polarfront* was a Norwegian weather ship located in the North Atlantic at 62° north, 2° east until the end of 2009. See “Polarfront” in *Store norske leksikon*, <https://snl.no/Polarfront> (accessed November 2021).

energy community has considered fluctuations in the mean wind direction only. The turbulence intensity is thus normally written as:

$$TI = \frac{\sigma_u}{\bar{u}}. \tag{2.13}$$

The numerical value of  $\sigma_u$  is sensitive to the length of the record considered. Traditionally, records of 10 min duration have been used in the wind industry. However, using longer records, e.g., 1 h, increases the computed value of  $\sigma_u$  as the wind spectra contain significant energy at low frequencies. Also, real wind data are never really stationary. Nybø et al. (2019) discuss ways to handle real wind data for use in the analysis of wind turbine dynamics.

Considering a short period of time, e.g., from 10 min to 1 h, the time history of the wind speed may be considered a stationary process. Several formulations of wind spectra are proposed. The most common spectra used for offshore conditions are the Kaimal, von Kármán, Davenport and Harris spectra; see, e.g., DNV (2021c). For example, the Kaimal spectrum may, according to IEC 61400 (2005), be written as:

$$S_k(f) = \sigma_k^2 \frac{A \frac{L_k}{U_{ref}}}{\left(1 + B \frac{fL_k}{U_{ref}}\right)^{5/3}}. \tag{2.14}$$

$f$  is the frequency and  $L_k$  is a length scale parameter.  $U_{ref}$  is the mean wind velocity at a reference height,  $z_r$ , e.g., the hub height. The index  $k$  refers to the velocity components:  $k = 1$  mean wind direction,  $k = 2$  lateral direction and  $k = 3$  vertical direction. IEC 61400 (2005) recommends the values given in Table 2.1 for the parameters, depending upon direction.

The length scale parameter is given as:

$$\Lambda_1 = \begin{cases} 0.7 z_r & \text{for } z_r < 60 \text{ m} \\ 42 \text{ m} & \text{for } z_r \geq 60 \text{ m} \end{cases}. \tag{2.15}$$

$A = 4$  and  $B = 6$  are recommended values. Note that in all wind spectral formulations, the high-frequency tail of the spectrum should be proportional to  $f^{-5/3}$ .

Table 2.1 Parameters to be used in the Kaimal spectrum according to IEC 61400 (2005)

Direction, $k$	1	2	3
Standard deviation, $\sigma_k$	$\sigma_1$	$\sigma_2 \geq 0.7\sigma_1$	$\sigma_3 \geq 0.5\sigma_1$
Integral length scale, $L_k$	$L_1 = 8.1\Lambda_1$	$L_2 = 2.7\Lambda_1$	$L_3 = 0.66\Lambda_1$

The wind spectrum may be divided into three ranges: a low-frequency range where large-scale turbulence is generated, denoted as the production range; a medium-frequency range where there is a balance between energy gained from the larger eddies and the energy lost to even smaller eddies, denoted as the inertial subrange; and a high-frequency range where the eddies are so small that the energy is lost in viscous dissipation, denoted as the Kolmogorov dissipation range. The order of magnitude length and time scales for each of these ranges are indicated in Figure 2.1. Experience shows that spectra such as, e.g., the Kaimal formulation represent the measured spectra well in the inertial subrange, at least in near neutral and unstable conditions. The length and time scales in the dissipation range are so small that they do not have any practical impact on wind turbines. However, the energy content in the lower range of the inertial subrange and in the production range may not be well represented by the “standard” spectra. This is a frequency range important to floating structures due to the low natural frequencies for such structures.

Figure 2.9 gives examples of the Kaimal spectrum. For frequencies above about 0.1 Hz, the slope of the spectrum is close to  $f^{-5/3}$ . Observe that changing the turbulence intensity while keeping the mean velocity causes a vertical shift in the spectral curve.

The formulation in [2.14] represents the spectrum in the main wind direction and uses the standard deviation in that direction,  $\sigma_u$ . For the lateral and vertical velocity components, the design standards propose the use of the same spectral formulation, but with modified standard deviations (see Table 2.1).

The turbulence intensity, as defined by [2.13], is in general assumed to decrease with increasing mean wind velocity. Nybø et al. (2019) and Nybø et al. (2020) investigated

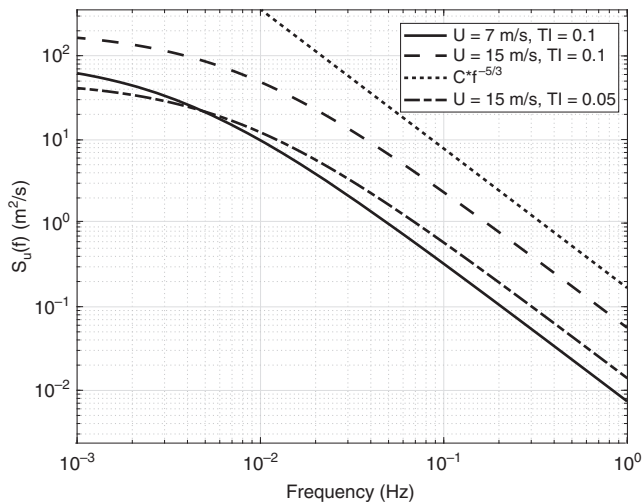


Figure 2.9 The Kaimal spectrum for the velocity in the mean wind direction according to IEC 61400 (2005). Reference height  $z_r = 100\text{ m}$ . Double logarithmic scale.



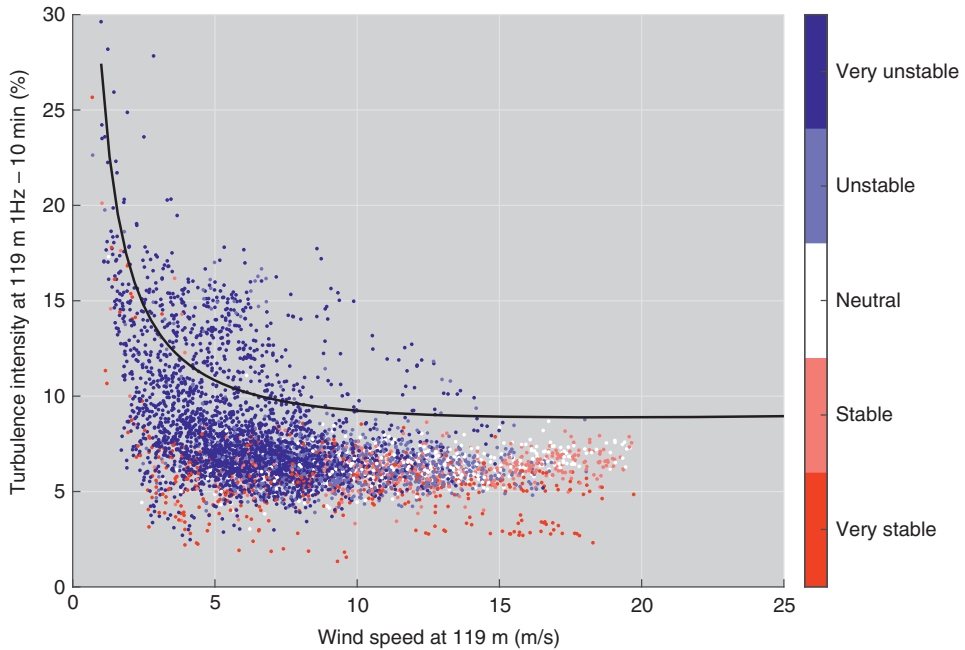


Figure 2.10 The turbulence intensity (TI) as a function of mean wind speed, from Nybø et al. (2020). The solid black line represents the 90th percentile as given in the IEC (2009) standard for offshore conditions with reference TI equal to 0.12. Reproduced from Nybø et al. (2020) under Creative Common Attribution License No. 5460641106526.

about one year of wind data from the offshore meteorological measurement platform FINO1 ([www.fino1.de/en/](http://www.fino1.de/en/); accessed July 2023). Careful quality control of the data was performed prior to the analysis. The quality control implies removing erroneous data due to spikes, missing samples, mast shadow effects etc., as well as implementing requirements related to the stationarity of the records. In Figure 2.10, turbulence intensities for the FINO1 data at 119 m above sea level are plotted for a large number of 60-min records. The TI values are averaged over six consecutive 10-min records sampled at 10 Hz. As shown in the figure, the turbulence intensity is sensitive to the stability of the atmospheric boundary layer. Nybø et al. (2020) used the classification of stability based upon the Obukhov length as given in Section 2.1.2.2. Figure 2.10 also includes turbulence intensities as recommended in the IEC standard 61400-3 (2009) for offshore wind turbines. These values are supposed to represent the 90th percentile of measured turbulence intensities. The 90th-percentile curves as given in the IEC standard decay monotonically with increasing wind speed. In Figure 2.11 the distribution of stability conditions in the data of Nybø et al. (2020) are plotted as function of mean wind speed. At very low and very high wind speeds, the few occurrences introduce large uncertainties in the distribution.

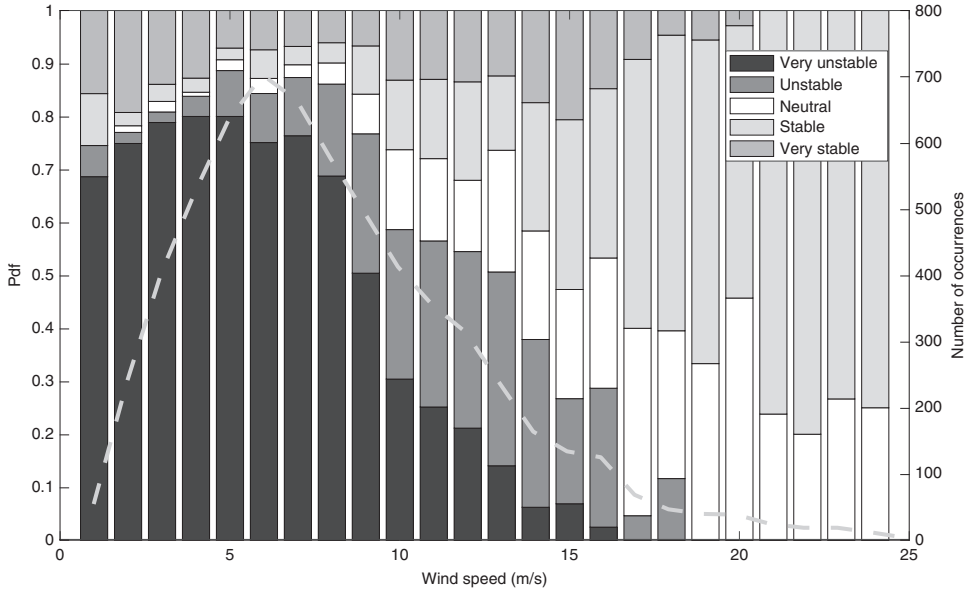


Figure 2.11 Atmospheric stability as a function of mean wind speed at 80 m above sea level. FINO1 data as processed by Nybø et al. (2020). The number of occurrences within each wind speed interval is given by the solid black line (right axis). The stability limits given in Section 2.1.2.2 are used. Copied from Nybø et al. (2020) under Creative Common Attribution 3.0 License No. 5460641106526.

In contrast to onshore conditions, the surface roughness offshore increases with wind speed. The IEC standard assumes the surface roughness can be solved iteratively from the expression  $z_0 = A_c / g [\kappa \bar{U}_{hub} / \ln(z_{hub} / z_0)]^2$ . Here,  $A_c$  is the Charnock parameter and  $\kappa$  is von Kármán’s constant. The standard deviation of the wind in the mean wind direction is written as  $\sigma_1 = \bar{U}_{hub} / \ln(z_{hub} / z_0) + 1.84 I_{15}$ . Here,  $I_{15}$  is the turbulence intensity at hub height at 15 m/s wind speed. In Figure 2.10, the IEC turbulence intensity curve is included, using  $A_c = 0.011$ ,  $\kappa = 0.4$  and  $I_{15} = 0.12$ , corresponding to Class C wind turbines. The surface roughness length varies in this case from 4.8E-07 at 1 m/s wind speed to 7.9E-04 at 25 m/s wind speed. The measurements reveal a large scatter in turbulence intensity for the various records analyzed. The turbulence intensity during unstable atmospheric conditions is in general higher than during neutral and stable conditions.

Classical theory describes how the wind shear over the ocean surface creates surface waves, starting from short, capillary waves. As the duration of the wind and or the fetch length increase, the waves become longer, ending up as long-periodic swells with periods beyond 15 s. The understanding of how waves cause variation of the wind speed over an ocean surface is less developed. The waves interact with

the wind field both by representing a wavy boundary condition and by a time-varying drag force. The drag force between the air and water is related to the relative velocity between the two media. As the water particles moves back and forth, a time-varying drag force will result. Kalvig (2014) studied the effect of the moving boundary and found that long swells could cause variation in the wind speed at vertical levels corresponding to the rotor of an offshore wind turbine. However, more research is needed to fully understand the impact of the waves on the wind field.

#### 2.1.2.5 Coherence

The above discussion on the turbulence spectra is confined to the velocity variation in time observed in one point. To compute the wind loads on a wind turbine, the velocity variations in space are also of importance. To describe the spatial variations, the coherence is used. The coherence of a wind field tells how the variation in wind speed at one point correlates to the wind speed at another point. Consider the rotor plane of a wind turbine. If the rotor diameter is small, it may be assumed that the wind speed is fully correlated over the rotor plane. This holds at least for the frequency ranges important for estimating the power production and dynamic loads. As seen from the power spectra in Figure 2.9, high frequencies correspond to low energy content.

As the diameter of the rotor is increased to beyond 200 m, the issue of correlation of the turbulence over the rotor plane becomes increasingly significant. The variation in the  $u$ -velocity over the rotor plane is obviously important. Due to the shear in the mean velocity profile, it is to be expected that the correlation in the  $u$ -velocity for points separated in the horizontal direction differs from the correlation between points separated in the vertical direction. Variations in the  $v$  and  $w$  turbulent velocity components over the rotor plane have had less attention but do also influence the rotor blade loads. In the following, the discussion is limited to the variation in the  $u$ -velocity component.

Consider two points, 1 and 2, separated by a distance  $r_{12}$ . The auto-spectra for the wind velocity at points 1 and 2 may be denoted  $S_{11}(f)$  and  $S_{22}(f)$ . Similarly, the cross-spectrum for the velocities at points 1 and 2 may be denoted  $S_{12}(f)$ . The coherence may now be written as:

$$\gamma(f, r_{12}) = \frac{S_{12}(f)}{\sqrt{S_{11}(f)S_{22}(f)}}. \quad [2.16]$$

The auto-spectra are real and positive, and in most cases almost equal in the two points considered. However, the cross-spectrum is in the general case a complex quantity. The coherence is therefore also complex, i.e., it contains information

about the phases or the time shift between the two time series considered. The real and imaginary parts of  $\gamma(f, r)$  are denoted the co-coherence and quad-coherence respectively. In most wind energy applications the absolute value of [2.16] is used as the coherence, i.e., the coherence is written as follows (Burton et al., 2011):

$$\text{coh}(f, r) = |\gamma(f, r_{12})| = \frac{|S_{12}(f)|}{\sqrt{S_{11}(f)S_{22}(f)}}. \quad [2.17]$$

In most wind standards an exponential coherence function is proposed, e.g., IEC (2005) proposes a coherence on the form:

$$\text{coh}(f, r) = \exp \left[ -12 \left( \left( \frac{fr}{U} \right)^2 + \left( 0.12 \frac{r}{L_k} \right)^2 \right)^{0.5} \right]. \quad [2.18]$$

Here,  $U$  is the mean wind velocity, to be taken at hub height.  $L_k = 8.1\Lambda_1$  is the coherence scale parameter; see [2.15]. [2.18] is supposed to be valid for the  $x$ -component of the velocity and describes the coherence between two points located in the same  $x - y$  plane (e.g., the rotor plane) at a distance  $r$ . From [2.18] it is observed that the coherence according to this formulation is always real and positive. It is also observed that the coherence tends to  $\exp(-1.44r/L_k)$  as the frequency tends to zero. For other coherence models, e.g., the Davenport model (Davenport, 1962), the coherence converges toward unity for zero frequency.

The above formulation of the coherence is to be combined with a model of the point spectrum of the wind, e.g. the Kaimal turbulence spectrum [2.14]. Using the ‘‘Sandia’’ method (Veers, 1988), a complete wind field satisfying the point spectrum as well as the coherence function may be generated. Further details are given below. Frequently, only the variation of the  $u$  - component of the wind is considered in these models.

#### 2.1.2.6 Mann’s Turbulence Model

Based upon a linearized version of the Navier–Stokes equations, Mann (1994) developed a tensor-based model for the spatial structure of the turbulence in the surface layer of the atmosphere. This is the original version of Mann’s turbulence model. The effect of the earth’s rotation, i.e., Coriolis forces, is ignored. To come up with a model for all three turbulent components of the wind field, several important simplifying assumptions are made. Key assumptions are that the air is assumed incompressible; further, a neutral stability of the atmosphere and a uniform shear of the mean velocity are assumed, i.e.:

$$\bar{u}(z) = z \frac{d\bar{u}}{dz}, \quad [2.19]$$

with  $d\bar{u}/dz$  constant. The model uses von Kármán's turbulence spectrum with isotropic turbulence as a starting point. The effect of shear is included by the so-called "rapid distortion theory" (RDT). The RDT describes how the sheared wind field distorts eddies. Eddies with rotation are either stretched or compressed along the axis of rotation depending upon the direction of rotation. Further, large eddies are assumed to live for longer than small eddies. Small eddies are assumed to be isotropic, simplifying the spectral tensor considerably. Large eddies are assumed to be anisotropic, causing the three components of the velocity fluctuations to differ and fulfil the relation:

$$\sigma_u > \sigma_v > \sigma_w. \quad [2.20]$$

Further, the ensemble average of the product of the horizontal and vertical turbulent velocities,  $\langle u'w' \rangle$ , becomes negative, as expected from the 2D boundary layer equations; see Appendix A.

If the fluctuation of the wind speed is measured at a fixed point in space, a time-history of the wind speed is obtained and, by spectral analysis, a frequency spectrum is obtained, as shown in Figure 2.9. In the spectral formulation by Mann (1994), a wave number spectrum is used rather than a frequency spectrum. The instantaneous wind speed variations along the  $x$ -axis at a certain point in time are considered. Computing the spectrum of these wind speeds,  $u(x)$ ,  $v(x)$ ,  $w(x)$ , a spectrum based upon wave number is obtained. Invoking the Taylor's frozen turbulence hypothesis implies that the turbulent structures are assumed to be moving downstream with the average wind speed, i.e.:

$$\mathbf{u}(x + \bar{u}\Delta t, y, z, t + \Delta t) = \mathbf{u}(x, y, z, t). \quad [2.21]$$

Bold types denote a vector. Denoting the spectrum based upon wave number  $F(k)$ , the relation between the frequency and wave number representation is given by  $S(f)df = F(k_1)dk_1$  with  $k_1 = 2\pi f/\bar{u}$ . Here,  $k_1$  is the wave number along the  $x$ -axis. The wave numbers along the  $y$  and  $z$  axes are independent of the mean velocity.

The model uses the covariance tensor as a basis, denoting the covariance tensor as:

$$R_{ij}(\mathbf{r}) = \langle u_i(\mathbf{x})u_j(\mathbf{x} + \mathbf{r}) \rangle, \quad [2.22]$$

where  $\mathbf{x} = (x, y, z)$  is the position vector,  $\mathbf{r}$  is a distance vector and  $u_i$  are the turbulent velocity components, and  $\langle \rangle$  denotes ensemble average. In a homogeneous flow field, the covariance tensor depends upon the absolute value of the distance only. Similarly, as the ordinary frequency spectrum is obtained from the

Fourier transform of the auto-correlation function, a spectral tensor is obtained from the Fourier transform of the covariance tensor, i.e.:

$$\Phi_{ij}(\mathbf{k}) = \frac{1}{(2\pi)^3} \iiint R_{ij}(\mathbf{r}) e^{-i\mathbf{k}\cdot\mathbf{r}} dr_1 dr_2 dr_3. \quad [2.23]$$

The integrals are taken from  $-\infty$  to  $+\infty$ .  $\mathbf{k} = (k_1, k_2, k_3)$  denotes the wave number vector. The spectral tensor is transformed to an orthogonal process, and the velocity field is then obtained from the Fourier transform of this process. Mann (1994) shows how the spectral tensor and  $F_i(k_i)$  can be obtained assuming an isotropic turbulence, using von Kármán's energy spectrum. Then, introducing a vertical shear, the spectral tensor is modified, and an anisotropic flow is obtained. The degree of anisotropy is determined by a parameter controlling the length of life of the eddies.

Three key parameters are used in Mann's (1994) formulation of the wind field: a length parameter  $L$  to describe the characteristic size of eddies; a parameter  $\Gamma$  to characterize the length of life of eddies; and a viscous dissipation rate for the turbulent kinetic energy.

Starting out with von Kármán's turbulence spectrum, the point spectrum for the  $u$ -velocity is obtained as:

$$F_u(k_1) = \frac{9}{55} \alpha \varepsilon^{\frac{2}{3}} \frac{1}{(L^{-2} + k_1^2)^{5/6}}. \quad [2.24]$$

Here,  $\alpha \varepsilon^{2/3}$  is the parameter characterizing the viscous dissipation rate for the turbulent kinetic energy.  $k_1$  is the wave number in  $x$ -direction.  $\varepsilon$  is the specific turbulent dissipation as given from the kinematic viscosity and the kinetic turbulent energy  $\varepsilon = \overline{v(du_i/dx_j)}$  (see Appendix A).  $\alpha$  is an empirical constant equal to approximately 1.7.

From [2.24] it is observed that the characteristic length,  $L$ , may be obtained from  $F_u(0)$ . However, Mann (1994) comments that the value of the spectrum at low wave numbers (low frequencies) is strongly influenced by non-stationarity and large-scale meteorological phenomena. He therefore suggests using the maximum of  $k_1 F(k_1)$  as reference. Considering the  $u$ -component of the velocity, it is found that:

$$L \simeq \frac{1.225}{k_{1\max}}, \quad [2.25]$$

where  $k_{1\max}$  corresponds to the maximum value of  $k_1 F(k_1)$ .

The linearization of the Navier–Stokes equations causes unrealistic behavior of the flow and the eddies to be distorted beyond what is physical realistic. Therefore, the parameter  $\Gamma$ , limiting the length of life of the eddies, is introduced. Eddies are

supposed to break up as time goes on and small eddies break up faster than large eddies. Mann (1994) applies an assumption that the length of life of the eddies may be written in the form:

$$\tau(k) \propto k^{-\frac{2}{3}} \Lambda \propto \begin{cases} k^{-2/3} & \text{for } k \rightarrow \infty \\ k^{-1} & \text{for } k \rightarrow 0 \end{cases} \quad [2.26]$$

$\Lambda$  is related to the hypergeometric function;<sup>6</sup> for details, see Mann (1994). The limit of  $\tau$  as  $k \rightarrow \infty$  is assumed valid in the inertial subrange. In the inertial subrange, [2.26] may be rewritten as a nondimensional lifetime as:

$$\beta(k) \equiv \frac{d\bar{u}}{dz} \tau(k) = (kL)^{-2/3} \Gamma. \quad [2.27]$$

$\Gamma$  is to be determined empirically. For  $\Gamma = 0$ , an isotropic flow is obtained, i.e.,  $\sigma_u = \sigma_v = \sigma_w$ . As  $\Gamma$  increases, the differences between the three standard deviations increase. In Figure 2.12, the relation between  $\Gamma$  and the variances in the three

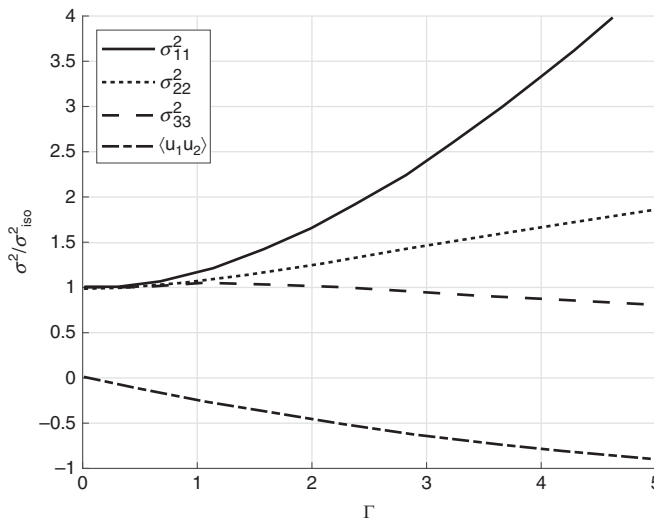


Figure 2.12 Relation between the parameter  $\Gamma$  controlling the length of life of eddies and the variances of the turbulence in the three directions as well as the covariance between horizontal and vertical velocity component. Reproduced from Mann (1994) with permission from the *Journal of Fluid Mechanics*, License No. 5431500056035.

<sup>6</sup> Hypergeometric functions represent solutions of a special group of second-order differential equations expressed as a series expansion; see, e.g., Wolfram MathWorld, <https://mathworld.wolfram.com/HypergeometricFunction.html> (accessed July 2023).

directions of the flow are shown. Further modifications to the model have been made by introducing a blocking effect, accounting for zero vertical velocity component at ground level.

In Mann (1998) and (1994), the above model was tested and the parameters estimated based upon full-scale measurements and for various model wind spectra. Cheynet, Jakobsen and Obhrai (2017) found, based upon offshore data at the FINO1 platform for wind velocities at 80 m above sea level and a wind speed range of 14–28 m/s, average values  $\Gamma = 3.7$ ,  $\alpha\varepsilon^{2/3} = 0.04 \text{ m}^{4/3} \text{ s}^{-2}$  and  $L = 70 \text{ m}$ . The estimated values for  $\Gamma$  and  $L$  are approximately constant over the range of velocities considered, while  $\alpha\varepsilon^{2/3}$  shows a marked increasing trend, from about  $0.02 \text{ m}^{4/3} \text{ s}^{-2}$  at the lowest velocity to  $0.07 \text{ m}^{4/3} \text{ s}^{-2}$  at the highest velocity.

To account for non-neutral atmospheric stability, Chougule et al. (2018) introduce a modification of the original Mann model. A linear vertical variation of the potential temperature is introduced. One or alternatively two extra parameters are needed for this model.

When applying the Mann model for wind field simulations, the tensor description of the wind field in the wave number domain is transformed to an instantaneous wind field in the  $(x, y, z)$  domain for the three turbulent components  $(u, v, w)$ . This is done by first transforming the spectral tensor,  $\Phi_{ij}(\mathbf{k})$ , into a set of orthogonal processes (functions). By Fourier transform and summation of these orthogonal functions, the wind field is obtained. Consistent with the frozen turbulence hypothesis, the wind turbine may be moved through this field to obtain a time-dependent inflow.

### 2.1.3 Numerical Generation of Wind Fields

Several options exist to generate wind fields that can be applied for analyzing wind turbines. First, an undisturbed wind field approaching a wind farm must be considered. Next, to analyze the wind field inside a wind farm, the effect of wakes has to be accounted for. Here, the generation for the free wind field is discussed briefly. The effect of wind turbine wakes is discussed in Chapter 9.

In Mann (1998), an efficient algorithm is given for computing the wind field according to the principles outlined above. One or more components of the turbulence may be generated assuming neutral atmospheric stability and constant vertical gradient of the mean wind speed. The result is a “wind field box” of specified size in  $(x, y, z)$ . Realistic spectral shape and variances for the three components of the wind speed as well as the covariance of the horizontal and vertical velocity components are obtained.

Veers (1984) and (1988) describes the “Sandia method” for generating a wind field. In this method the three turbulent components are assumed to be uncorrelated



and can thus be generated independently. The time histories of the wind speed at several points in a plane perpendicular to the mean wind direction are considered. The plane may coincide with the rotor plane. The time histories of the wind speed in each point are supposed to be Gaussian and the point spectrum of the wind in each point (point number  $n$  of total  $N$ ) is given by a frequency spectrum,  $S_n(f)$ . In most cases the spectrum is assumed equal for all the points considered. The subscript  $n$  is thus omitted in the following. The spectrum is represented by a summation of  $M$  frequency components, each with amplitude  $\sqrt{2S(f_m)\Delta f}$ . Here,  $\Delta f$  is the frequency increment and a single-sided spectrum is assumed. The wind speeds at two points are not independent. The degree of correlation depends upon the distance between the points. Consider the rotor plane and denote two points in the plane,  $j$  and  $k$ , with the coordinates  $(x, y_j, z_j)$  and  $(x, y_k, z_k)$ . The cross-spectrum for the wind speed between the two points can be written as:

$$S_{jk}(f_m) = \gamma(f_m, \Delta r_{jk}) \sqrt{S_{jj}(f_m)S_{kk}(f_m)}. \quad [2.28]$$

$S_{jj}(f_m)$  is the auto-spectrum (point spectrum) in point  $j$ . As mentioned above,  $S_{jj}(f_m) = S_{kk}(f_m)$  is normally assumed.  $\Delta r_{jk}$  is the distance between the two points. Note that the coherence depends upon the distance between the points and does not distinguish between vertical and horizontal separation. Taylor's frozen turbulence hypothesis is applied, i.e., the turbulent eddies, the velocity variations, are moved downstream with the mean wind velocity. Veers (1984) assumed that the coherence function is real and positive. This assumption was justified by the fact that within the typical rotor sizes considered, the phase shift in the velocity components over the rotor, even in vertical direction, is small. The assumption simplifies the computations significantly. The assumption of a real and positive coherence function contrasts with the results that are obtained by Mann's formulation, which may result in negative cross-spectra and an imaginary part of the cross-spectra different from zero.

The time history of the wind speed is to be generated in  $N$  points in the rotor plane. Each time history is assumed to be a filtered white noise process, obtained by summation of the  $M$  frequency components. Further, the correlation between the time series shall satisfy [2.28]. For each frequency, the spectral matrix  $\mathbf{S}(f_m)$  contains the spectral value for all combinations of  $j$  and  $k$  altogether  $N^2$  values. As the distance between two points is equal in both directions,  $\mathbf{S}(f_m)$  is symmetric. In general,  $\mathbf{S}(f_m)$  may be rewritten as the product between a complex transformation matrix and the transposed of its complex conjugate, i.e.:

$$\mathbf{S}(f_m) = \mathbf{H}(f_m)\mathbf{H}^{*T}(f_m). \quad [2.29]$$

As  $\mathbf{S}(f_m)$  is assumed real,  $\mathbf{H}(f_m)$  is real and equal to its complex conjugate. It is now assumed that  $\mathbf{H}(f_m)$  is a lower triangular matrix. The non-zero values may then be determined by a set of recursive equations (see Veers, 1984), i.e.:

$$\begin{aligned}
 H_{11} &= S^{1/2} \\
 H_{21} &= S_{21}/H_{11} \\
 H_{22} &= (S - H_{21}^2)^{1/2} \\
 H_{31} &= S_{31}/H_{11} \\
 &\vdots \\
 H_{jk} &= \left( S_{jk} - \sum_{l=1}^{k-1} H_{jl}H_{kl} \right) / H_{kk} \\
 H_{kk} &= \left( S - \sum_{l=1}^{k-1} H_{kl}^2 \right)^{1/2}
 \end{aligned}
 \tag{2.30}$$

This matrix is unique for each frequency,  $f_m$ . Veers (1988) states that “the elements of  $\mathbf{H}$  may be thought of as weighting factors for the linear combinations of  $N$  independent, unit-magnitude, white noise inputs that will yield  $N$  correlated outputs with the correct spectral matrix. Each row of  $\mathbf{H}$  gives the contribution of all the inputs to the output at point  $k$ .”

The harmonic components along the diagonal of  $\mathbf{H}$  at each frequency  $f_m$  are assumed to be uncorrelated. This is obtained by assuming each component has an independent, random phase  $\theta_{jm}$  between 0 and  $2\pi$ . A unit amplitude diagonal matrix  $\mathbf{X}$  is thus introduced with the elements:

$$X_{jj}(f_m) = e^{i\theta_{jm}}.
 \tag{2.31}$$

The harmonic component of the velocity with frequency  $f_m$  in point  $n$  may thus be written as a linear sum of the contribution from the point itself and its neighbors, accounting for the lower diagonal structure of  $\mathbf{H}$ :

$$V_n(f_m) = \sum_{k=1}^n H_{nk}(f_m)X_{kk}(f_m) = \sum_{k=1}^n H_{nk}(f_m)e^{i\theta_{km}}.
 \tag{2.32}$$

Having established all the frequency components for each point, the time-history is obtained by a Fourier transform of  $V_n$ . For details and an example of usage, see Veers (1988).

In Nybø et al. (2021), the coherence of the  $u$ -component of the velocity as computed by various methods is compared. The results are illustrated in

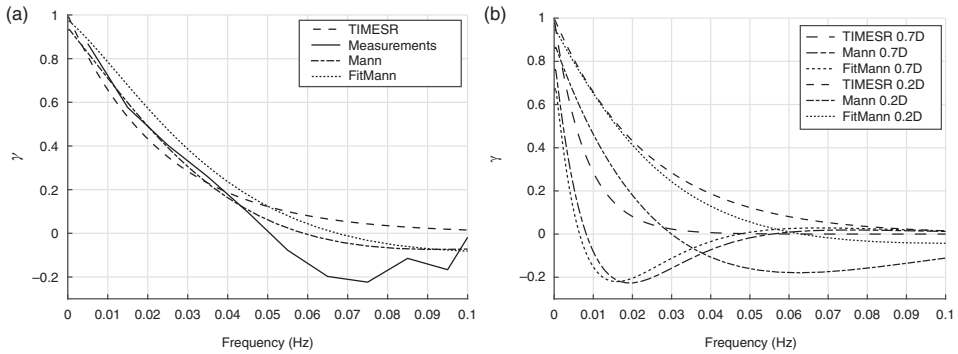


Figure 2.13 Computed coherence based upon offshore measurements and various wind field models. Left: vertical co-coherence of the  $u$ -component computed for 40 m vertical separation. Right: horizontal co-coherence of the  $u$ -component computed for 36 m (0.2D) and 125 m (0.7D) horizontal separation. Copied from Nybø et al. (2021) under Creative Commons Attribution 3.0 license.

Figure 2.13. The wind fields are computed by Mann’s method, as described, using standard parameters as recommended from the design standards and fitting the turbulence level to measurements. Further, a version of Mann’s model with fitting of the spectral shape is employed, known as “FitMann” (Cheynet, 2019). “TIMESR” uses the Sandia method, as described, with input from wind measured at three different vertical levels. The Davenport exponential coherence function is used with parameters fitted to the measurements. The specific condition considered in Figure 2.13 has close to neutral atmospheric stability. The vertical coherence is also computed directly from the measurements. The measurements are from an offshore meteorological mast, FINO1 (Nybø et al., 2019; Nybø et al., 2020).

From Figure 2.13 it is observed that the measured vertical co-coherence is negative in some ranges of frequencies. The observed negative co-coherence is partly captured by the two Mann’s models. This is not the case for the Davenport coherence model, in which the co-coherence is forced to be positive. For the horizontal coherence, no measurements are available. However, Mann’s model still predicts negative co-coherence in some ranges of frequencies. Measurements also show quad-coherence different from zero, in particular in the vertical direction. A vertical quad-coherence different from zero is also obtained by Mann’s model. However, present practice in wind turbine design frequently ignores the quad-coherence.

In addition to the methods discussed above, numerical methods based upon solving the Navier–Stokes equations are used. Still, most of the methods available are too computationally demanding to be used directly in the design process.

However, for calibrating more simplistic methods and in studies of special flow phenomena, these methods are very useful.

The simplest version is the so-called Reynolds-averaged Navier–Stokes (RANS) solvers. As the name indicates, these methods average out all turbulent variations and give a picture of the time-averaged flow only. The effect of turbulence is parameterized to ensure proper shear and dissipation of energy in the flow. Such methods are of limited value in considering wind turbines.

The most relevant Navier–Stokes solver methods are the large-eddy simulation (LES) methods. In this approach the turbulent structures with sizes above a certain limit are resolved in the numerical model, while the smaller-scale turbulence is parameterized to ensure proper turbulent dissipation of energy. Two frequently used implementations are the Parallelized Large-Eddy Simulation Model (PALM; Maronga et al., 2015) and the Simulator fOr Wind Farm Application (SOWFA; see, e.g., Churchfield et al., 2012). These computational tools typically start from a meso-scale wind field that is refined by using a finer-grid scale in the wind farm area, and this locally refined flow model is coupled with a wind turbine model to compute power production, loads and wakes behind the turbines.

The starting point for the models is the three-dimensional momentum equation driven by a horizontal pressure gradient and accounting for Coriolis forces due to the rotation of the earth. The air may be considered incompressible, but with the buoyancy effect included by assuming that the vertical variation of the density of the air follows the variation in potential temperature, the so-called Boussinesq approximation. The density of the air at some vertical level,  $z$ , may thus be written as:

$$\rho(z) = \rho(z_r) \left[ 1 - \frac{\bar{\theta}(z) - \bar{\theta}(z_r)}{\bar{\theta}(z_r)} \right]. \quad [2.33]$$

Here,  $z_r$  is some vertical reference level.

The turbulent fluctuations of the velocities are split into resolved variations and sub-grid variations. The closure of the sub-grid problem is not trivial and several closure methods exist (Maronga et al., 2015). Also, coupling the coarse meso-scale<sup>7</sup> model to a finer micro-scale model represents a challenge. This may be performed by a one-way or a two-way coupling.

<sup>7</sup> The meso-scale has a range from a few kilometers to several hundred kilometers. The micro-scale ranges from a few hundred meters to a few kilometers.

### Nested Computational Domains in Numerical Simulation of Wind Fields

To obtain a stationary flow field, a “precursor” simulation may be performed. The simulation is run with a given horizontal pressure gradient, a surface roughness and, for example, a constant heat transfer from the ground. At the upper boundary, a “free slip” condition is normally used. To simulate the capping inversion layer at the top of the atmospheric boundary layer, a fixed positive gradient of the potential temperature may be applied in the upper part of the computational domain. In the precursor run, the flow will gradually change from the initial flow (e.g., a homogeneous flow) to a flow with proper shear, turbulence and temperature profile. The result from this precursor run may then be used as an input to a more refined model with wind turbines. An example of a precursor run is shown in Figure 2.14. Here, a flow field with an extent of 5.12 km x 5.12 km x 1.28 km is used. Thus, about 34 million grid cells are used in the domain. To obtain the wanted turbulence intensity at nacelle level, in this case approximately 100 m above sea level, a surface roughness length of 0.0001 m is used. Neutral atmospheric stability is obtained by using zero heat flux from the ground. To include turbines in the flow, a refined grid is needed in the vicinity of the turbines and a stepwise reduction in the size of the grid size is used. In Figure 2.15, an example of a such stepwise reduction of the grid size is shown. The placement of the turbines is also illustrated. The technique of including more refined grids inside a coarser grid is called nesting. In the present example, the inner domain has a grid size of 2.5 m. By using nesting as illustrated in Figure 2.15, the total number of grid cells will increase to approximately 100 million.

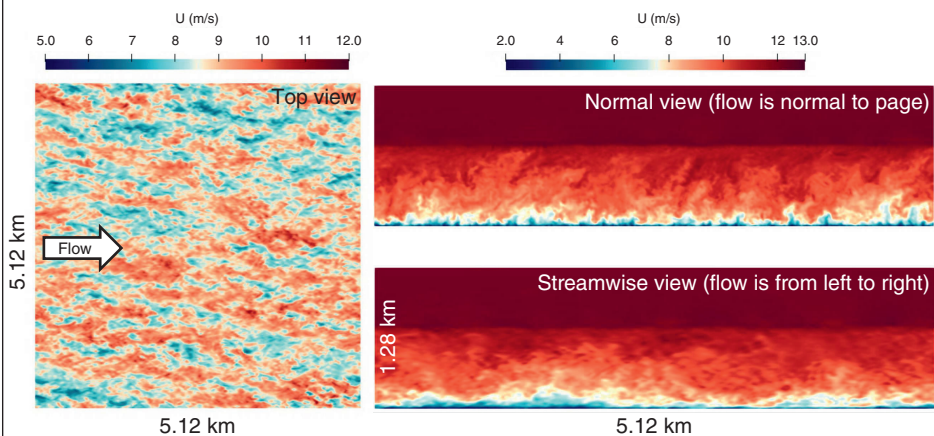
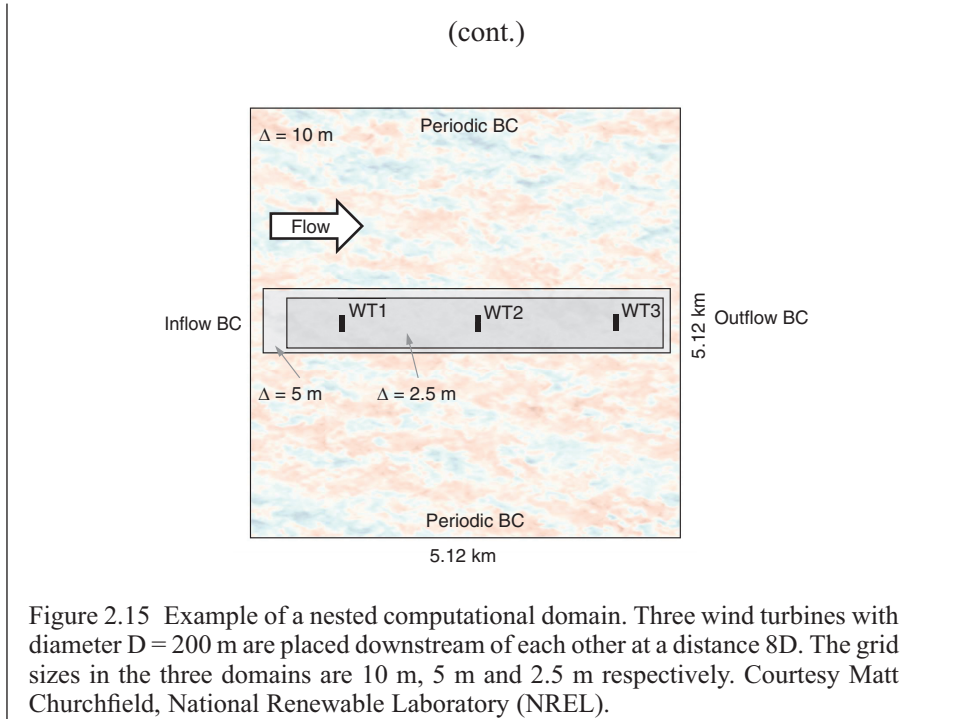


Figure 2.14 Example of result from a precursor run of an offshore wind field. Left: instantaneous flow velocities 140 m above sea. Right: instantaneous flow velocities in stream-wise and normal directions relative to the flow. The boundary layer is neutral and stable capped. Grid resolution 10 m. Courtesy Matt Churchfield, National Renewable Laboratory (NREL).



### 2.1.4 Long-Term Wind Statistics

In the design of wind turbines and to estimate the expected energy production, a long-term statistic of the mean wind speed is required. For several locations around the world, historical time series for the key meteorological data are available for several years. The data are given on a horizontal grid and at several vertical levels. Examples of such datasets are NORA10 and its updated version NORA10EI (Haakenstad et al., 2020) and NORA3 (Haakenstad et al., 2021). Both NORA10 and NORA3 cover significant parts of the North Sea, Norwegian Sea and Barents Sea. NORA10 has a temporal resolution of 3 h and a horizontal grid of approximately 10 km x 10 km. NORA3 has a finer temporal and spatial resolution of 1 h and 3 km x 3 km. The datasets cover about 50 and 30 years respectively. The models are based upon downscaling from larger-scale meteorological models. Such datasets are called hindcast data as they are based upon numerical simulation of historical weather with observations assimilated into the simulations. In addition to wind data, pressure, wave and temperature information is available.

Figure 2.16 shows an example of the long-term distribution of the 10 min mean wind velocity 100 m over the sea level at a specific location in the North Sea (the proposed wind field area “Utsira North”). The data were obtained over 15 years using the NORA3 database. The three-parameter Weibull probability distribution is normally used to

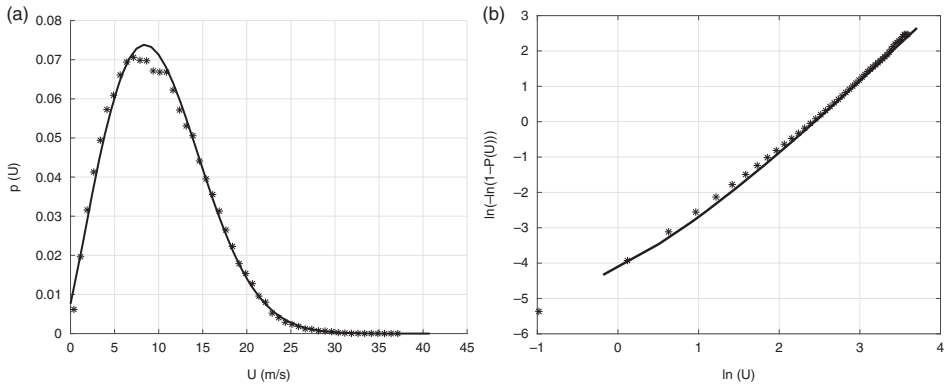


Figure 2.16 Example of distribution of hourly 10 min average wind speeds 100 m above sea level in the North Sea. Fifteen years of data are used. Left: probability distribution. Stars: binned data, 50 bins; solid line: fitted three-parameter Weibull distribution. Right: cumulative distribution plotted on Weibull scale. Data from the NORA3 database (Haakenstad et al., 2021).

represent the long-term distribution of the mean wind velocity. The three-parameter Weibull probability density and cumulative distributions for a variable  $x$  are written as:

$$\begin{aligned}
 p(x) &= \frac{\beta}{\alpha} \left(\frac{x - \gamma}{\alpha}\right)^{\beta-1} e^{-\left(\frac{x - \gamma}{\alpha}\right)^\beta} \\
 P(x) &= 1 - e^{-\left(\frac{x - \gamma}{\alpha}\right)^\beta}
 \end{aligned}
 \tag{2.34}$$

Here,  $\alpha (>0)$  is the scale parameter, used to normalize the variable;  $\gamma (\leq x)$  is the location parameter, used to define a lower threshold for the variable; and  $\beta (>0)$  is the shape parameter, defining the shape of the distribution. For the data shown in Figure 2.16, the parameters are estimated as  $\alpha = 12.31$ ,  $\gamma = -0.848$  and  $\beta = 2.18$ . The distribution may be used to estimate extreme values with certain return periods; for details, see Section 2.3.2. By combining the long-term distribution of the mean velocity with the power production characteristics of the wind turbine, the statistics of the power production at a certain location are obtained. The power characteristic is discussed in Section 3.8. Similarly to the long-term yearly distribution of the wind speed, seasonal distributions are frequently used.

The instantaneous wind velocity differs over the ocean area. Figure 2.17 illustrates the 10 min mean wind speed during the extreme weather event “Dagmar” in 2011. Large spatial variations in wind speed are observed. Such spatial variations are also present during more normal weather situations. Knowledge about the spatial correlation of the mean wind velocities may be utilized to mitigate the intermittent nature of wind power; see, e.g., Solbrekke et al. (2020).



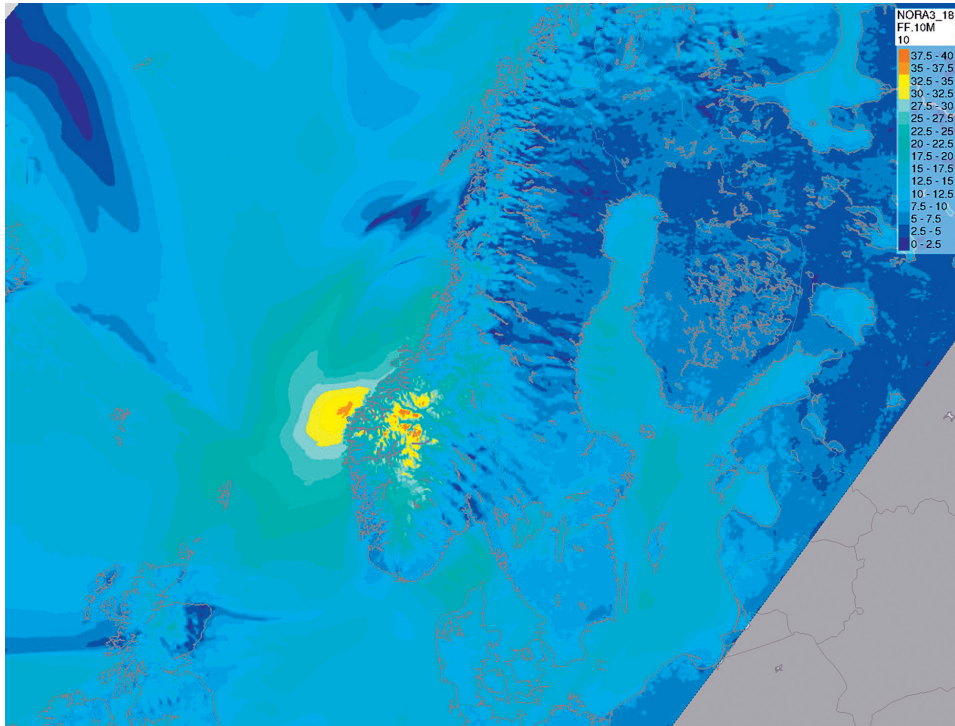


Figure 2.17 Wind speed during the extreme weather event “Dagmar,” December 25, 2011. 10 min mean wind speed in m/s at 21:00 UTC. Courtesy the Norwegian Meteorological Institute.

### 2.1.5 Wind Measurements

Several techniques exist for measuring wind speed. They differ in the ability to measure wind direction, resolve high-frequency wind components and measure the different directional components of the turbulent wind. Some techniques also average the wind speed over a volume. In the following sections, some of the most common techniques are discussed in brief.

#### 2.1.5.1 Cup Anemometers

Cup anemometers (Figure 2.18) are widely used for wind measurements. The main principle relies upon the fact that the drag force of a conical cup is larger for flow into the cup than for flow from the back of the cup. In the “Risø” version of the cup anemometer, three cups are mounted on a vertical axis. The rotational resistance in the bearings is very low, causing the rotation to start at very low wind speeds. The rotational speed of the cup anemometer is close to proportional to the wind speed. The relation between wind speed and rotational speed is discussed in some detail in





Figure 2.18 Cup anemometer with three cups. Photo by Stephan Kral, University of Bergen.

Section 3.5, where a cup anemometer is considered in a power production context. Cup anemometers are considered accurate but have some disadvantages, e.g., they measure the total horizontal wind speed only and give no information about wind direction. To obtain the wind direction, a separate wind vane must be used. As the rotor system has a certain inertia, high-frequency wind speed variations will not be measured. In turbulent wind, the average wind speed tends to be overestimated. This is because the drag characteristic of the cups will cause the rotor to rapidly speed up during a wind speed increase, but the rotational speed will reduce more slowly during wind speed decrease. The cup anemometer must be mounted on a mast. Care must thus be taken to avoid shadow or speed-up effects due to the mast and mounting system. Wind directions affected by the mast and mounting system should be removed from the subsequent data analysis.

#### 2.1.5.2 Sonic Anemometers

Sonic anemometers use ultrasonic senders and receivers. Consider the two combined sender and receiver sensors illustrated in Figure 2.20. The time a sound signal requires to move from one sensor head to the other is given by:

$$T_{AB} = \frac{L}{c + U_{AB}} \quad [2.35]$$

$$T_{BA} = \frac{L}{c - U_{AB}}$$

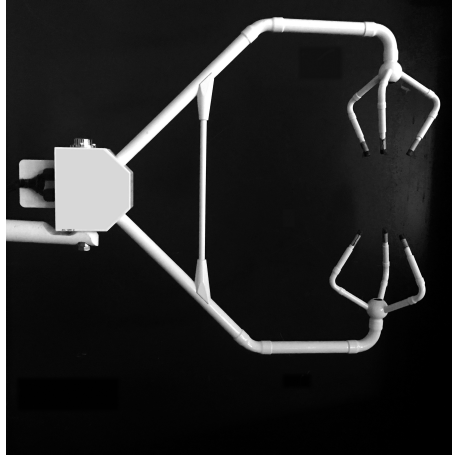


Figure 2.19 Example of a three-component sonic anemometer. Photo by Stephan Kral, University of Bergen.

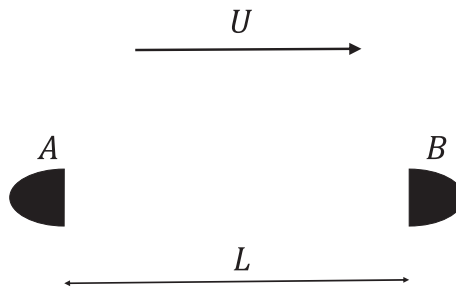


Figure 2.20 Principle of a sonic anemometer. Sensor heads A and B are located a distance  $L$  apart.

Here,  $U_{AB}$  is the component of the wind velocity along a straight line between the sensors  $A$  and  $B$ . The distance between the sensors is  $L$ . The speed of sound is  $c$ . Rearranging [2.35], the following relations are obtained:

$$U_{AB} = \frac{L}{2} \left( \frac{1}{T_{AB}} - \frac{1}{T_{BA}} \right) \quad [2.36]$$

$$c = \frac{L}{2} \left( \frac{1}{T_{AB}} + \frac{1}{T_{BA}} \right)$$

It is observed that the expression for the wind speed is not dependent upon the speed of sound and that the speed of sound is obtained as well. By locating sensors in three

orthogonal directions, all three components of the wind vector can be measured. Figure 2.19 shows an example of a three component sonic anemometer. Compared to the cup anemometer, the sonic anemometer has the advantage of a very high frequency resolution and the possibility of measuring all components of the wind. As for the cup anemometer, one must be aware of possible shadow effects of the mast and mounting arrangement. Experience shows that the sonic anemometer may give erroneous results during rainy weather; see, e.g., Nybø, et al. (2019).

### 2.1.5.3 Lidar

The LIDAR measurement technique is a remote sensing technique. The name LIDAR originates from an abbreviation of “light-based radar” or “light detection and ranging.” A simplistic view of the basic principle is illustrated in Figure 2.21. A narrow beam of laser (monochrome) light is sent out from the LIDAR unit. The light is scattered by aerosols in the air and some of the light is back-scattered into the LIDAR’s receiver system, which utilizes the Doppler effect. By detecting the change of frequency in the back-scattered light, the speed of the aerosol particles, i.e., the wind speed in the direction of the laser beam,  $U_s$ , is obtained. As the light beam has a finite angle and the duration of the analyzed scattered signal has a finite duration, the velocity obtained is a weighted average over a volume, as illustrated in Figure 2.21. Typical averaging lengths in the direction of the beam are in the order of tens of meters. Assuming no mean vertical component of the wind speed, the

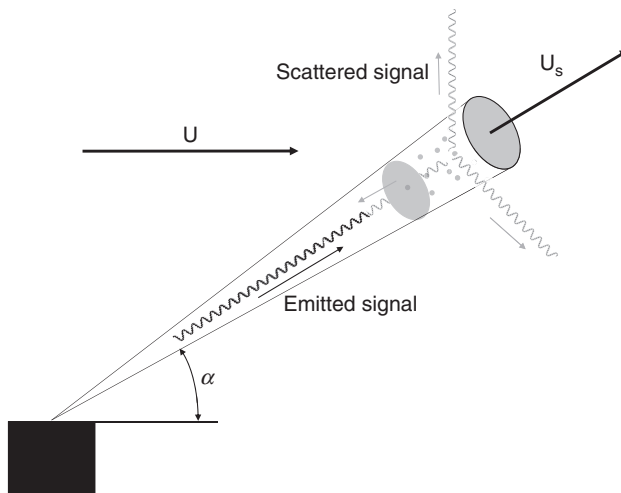


Figure 2.21 Basic principle of LIDAR. Some of the emitted light is back-scattered from the aerosol particles in the air between the two planes. From the frequency shift in the back-scattered signal, the component of the wind velocity in the direction of the beam,  $U_s$ , may be determined.

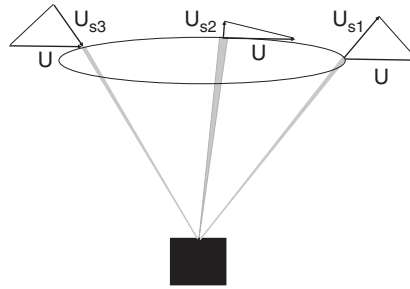


Figure 2.22 Example of circular sweeping pattern of the laser beam to obtain both components of the horizontal mean wind speed.  $U$  is the total horizontal wind speed;  $U_{si}$  is the measured component of the wind speed in azimuthal angle  $\beta_i$ .

horizontal component of the mean wind speed in the vertical plane described by the laser beam is obtained as  $U_\beta = U_s / \cos\alpha$ .  $U_\beta$  is the horizontal wind speed component in direction  $\beta$  and  $\alpha$  is the angle between the laser beam and the horizontal plane.

To obtain the total horizontal wind speed, at least two orthogonal measurements must be performed. In practice, to obtain the total horizontal velocity, a circular sweeping pattern of the laser beam can be used, as illustrated in Figure 2.22. The laser beam measures the velocities  $U_{si}$  at a number of azimuthal angles  $\beta_i$ . The relation between the mean horizontal wind velocity,  $\bar{U}$ , and the measured speed in the direction of the laser beam is thus:

$$U_{si} = \bar{U} \cos(\beta_i - \beta_0) \cos\alpha. \quad [2.37]$$

Here,  $\beta_0$  is the mean direction of the wind. By measuring for several values of  $\beta_i$ , the mean wind speed and the mean direction are obtained. A key assumption used to obtain the mean wind speed by this approach is that the wind field is homogeneous over the sweeping area.

Other remote measurement techniques utilize sound (SODAR) and microwaves (RADAR) to obtain the wind velocity. The sound signals are scattered by temperature differences in the air. Assuming that such temperature structures are advected with the mean wind speed, the wind speed in the direction of the sound wave is obtained by considering the frequency shift between emitted and reflected sound (for details, see, e.g., Lang and McKeogh, 2011). Microwave radars may be used in combination with SODAR. The radar signals may interfere with the sound waves through the so-called Bragg effect. This makes it possible to determine temperatures in addition to velocities.

## 2.2 Ocean Waves

### 2.2.1 Introduction

This section will give the classical linear description of gravity waves in the ocean. This is the most common wave description used in the computation of wave loads on marine structures. To compute the loads on marine structures, we must know about the surface elevation of the waves as well as the velocity and acceleration fields in the water below the free surface. An important feature of the linear description is the principle of superposition. This makes it possible to describe a complex sea state by a summation of harmonic components. Some issues related to the nonlinearity of waves will also be addressed. Fixed offshore wind structures are normally located at water depths where the sea bottom “is felt” by the waves. Such finite water depth conditions are important for the wave kinematics.

More details on the modeling of ocean waves may be found in World Meteorological Organization (2018), Mork (2010), Faltinsen (1990) and DNV (2021c).

### 2.2.2 Assumptions

Ocean gravity waves may be modeled under the assumptions that water is incompressible and that capillarity effects and viscous effects may be ignored. In the following, constant density is also assumed. This implies that we are not considering internal waves. Such waves may occur in cases with water of low salinity on top of more saline water. However, internal waves are normally not considered in the design of offshore wind turbines.

To derive the governing equations for linear-gravity waves, it is assumed that the velocity field can be described by a velocity potential  $\phi$  and that the fluid velocities are obtained from the gradients of the velocity potential:

$$\mathbf{u} = \nabla\phi. \quad [2.38]$$

Here,  $\mathbf{u} = (u, v, w)^T$  is the velocity vector given by the components of the velocity in the  $x, y$  and  $z$  directions. The  $(x, y, 0)$  plane is at the mean free surface.  $z$  is vertical, zero at the mean free surface and positive upwards; see Figure 2.23. Under the condition that the fluid is incompressible and irrotational, the potential will satisfy Laplace equation throughout the fluid:

$$\nabla^2\phi = \frac{\partial^2\phi}{\partial x^2} + \frac{\partial^2\phi}{\partial y^2} + \frac{\partial^2\phi}{\partial z^2} = 0. \quad [2.39]$$

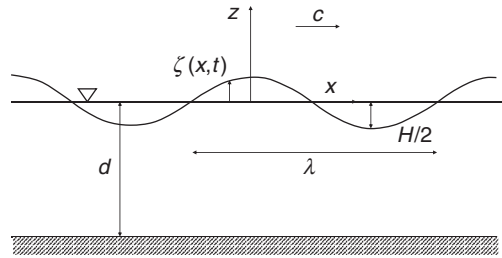


Figure 2.23 Notations used in describing the linear ocean gravity waves. The waves propagate in positive  $x$ -direction. Surface elevation  $\zeta(x, t)$  is shown at  $t = 0$ .

### 2.2.3 Solution

To solve the above Laplace equation, proper boundary conditions must be imposed. To simplify the problem, it is assumed that the waves propagate in positive  $x$ -direction, so the velocities in  $y$ -direction are zero,  $\frac{\partial \phi}{\partial y} = 0$ . The following boundary conditions are then to be imposed at the sea bottom and at the free surface.

Under the condition that the bottom is horizontal, zero vertical velocity must be required at the bottom, i.e.:

$$\frac{\partial \phi}{\partial z} = 0 \quad \text{at } z = -d. \quad [2.40]$$

At the free surface, two conditions are to be imposed: one kinematic and one dynamic. The kinematic condition implies that particles, once located at the free surface, will remain there, i.e., the particles on the free surface must follow the motion of the free surface. This may be expressed as:

$$\frac{\partial \zeta}{\partial t} = \frac{\partial \phi}{\partial z} - \frac{\partial \phi}{\partial x} \frac{\partial \zeta}{\partial x} \quad \text{at } z = \zeta. \quad [2.41]$$

Here,  $\zeta$  is the free surface elevation. The first term is the vertical velocity of the free surface at a specific  $x$ -position. This vertical velocity must equal the two terms on the right-hand side, the first one being the vertical velocity of the water and the second being the horizontal velocity of the water multiplied by the slope of the surface. This condition is to be satisfied at the instantaneous free surface level.

The dynamic free surface condition is the requirement of constant pressure on the free surface, equal to the atmospheric pressure. Invoking Bernoulli's equation, we may write:

$$\rho \frac{\partial \phi}{\partial t} + \frac{\rho}{2} \left[ \left( \frac{\partial \phi}{\partial x} \right)^2 + \left( \frac{\partial \phi}{\partial z} \right)^2 \right] + \rho g \zeta = C \quad \text{at } z = \zeta. \quad [2.42]$$

The first term is the pressure related to the acceleration of the fluid, the second term is due to the velocities and the third term is the hydrostatic contribution.

The kinematic and dynamic boundary conditions on the above forms imply a nonlinear solution of the problem. Exact analytical solutions of this problem do not exist. However, several approximate solutions are derived, in particular the class of Stokes wave solutions that are found by a series expansion of the problem. Classic solutions are Stokes second-order and Stokes fifth-order waves; see, e.g., Sarpkaya and Isaacson (1981). These classical solutions assume an infinite train of equal waves. Each wave is also symmetric in the sense that the front and back slope of the wave crest are equal. This is not in accordance with the geometry of real steep waves.

To obtain a linear solution of the above boundary value problem, the following approximations are introduced. It is assumed that the slope of the waves is small and that the boundary conditions may be satisfied at  $z = 0$  rather than at  $z = \zeta$ .

The small slope approximation implies that the second term on the right-hand side of [2.41] is much smaller than the first term and is thus ignored. Similarly, the velocity-squared terms in [2.42] are ignored. [2.41] and [2.42] are in linearized form thus written as:

$$\begin{aligned} \frac{\partial \zeta}{\partial t} - \frac{\partial \phi}{\partial z} &= 0 \quad \text{at } z = 0 \\ \frac{\partial \phi}{\partial t} + g \zeta &= 0 \quad \text{at } z = 0 \end{aligned} \quad [2.43]$$

The constant in the Bernoulli equation may be set to zero. By taking the time derivative of the dynamic boundary condition and combining it with the kinematic condition, the two equations may be combined into one, which constitutes the linearized free surface boundary condition:

$$\frac{\partial^2 \phi}{\partial t^2} + g \frac{\partial \phi}{\partial z} = 0 \quad \text{at } z = 0. \quad [2.44]$$

The linearized free surface elevation is obtained as:

$$\zeta = -\frac{1}{g} \left( \frac{\partial \phi}{\partial t} \right)_{z=0}. \quad [2.45]$$

It is further assumed that the solution shall represent a harmonic progressive wave. The Laplace equation [2.39] is combined with the linear boundary conditions in [2.40] and [2.45] and the solution may be written as:

$$\phi = i \frac{gH}{2\omega} \frac{\cosh[k(z+d)]}{\cosh(kd)} e^{i(\omega t - kx)}. \quad [2.46]$$

Here,  $k = 2\pi/\lambda$  is the wave number and  $\lambda$  is the wavelength.  $\omega = 2\pi/T$  is the wave angular frequency and  $T$  is the wave period.  $d$  is the water depth.  $H$  is the double amplitude for the wave, equal to twice the single amplitude,  $\zeta_A$ , under the assumption of linear waves. For nonlinear waves, however, the height of the wave crest and the depth of the wave trough differs, and it is convenient to use the distance from trough to crest, the wave height, as a measure. It is implicit that it is the real part of the quantities which has physical meaning. The free surface elevation is obtained as:

$$\zeta = \text{Re} \left\{ \frac{H}{2} e^{i(\omega t - kx)} \right\} = \zeta_A \cos(\omega t - kx). \quad [2.47]$$

As the water depth tends to infinity, the potential may be written as:

$$\phi = i \frac{g\zeta_A}{\omega} e^{kz} e^{i(\omega t - kx)} \quad \text{as } d \rightarrow \infty. \quad [2.48]$$

A frequently used assumption is that the deep-water formulation may be used if the water depth is greater than half the wavelength. Another result is the so-called dispersion relation, the relation between the wave number and the wave (angular) frequency:

$$\omega = \sqrt{kg \tanh(kd)}. \quad [2.49]$$

In the limits  $d \rightarrow 0$  and  $d \rightarrow \infty$ , the dispersion relation becomes:

$$\begin{aligned} \omega &\rightarrow k\sqrt{gd} \quad \text{as } d \rightarrow 0 \\ \omega &\rightarrow \sqrt{kg} \quad \text{as } d \rightarrow \infty \end{aligned} \quad [2.50]$$

The speed of the wave, the wave celerity or the phase speed is given as  $c = \lambda/T = \omega/k$ . In the general case, the wave celerity is given as:

$$c = \frac{\omega}{k} = \sqrt{\frac{g}{k} \tanh(kd)}. \quad [2.51]$$



In the shallow and deep-water cases, the following limiting values are obtained (for more details, see Section 2.2.5):

$$\begin{aligned} c &\rightarrow \sqrt{gd} & \text{as } d \rightarrow 0 \\ c &\rightarrow \frac{g}{\omega} & \text{as } d \rightarrow \infty \end{aligned} \quad [2.52]$$

We observe that the speed of the waves becomes independent of wave period as the water depth tends to zero. This is the case as long waves approaches a shallow beach. In deep waters, waves with long periods move faster than those with short periods. If we observe the wave field in the open ocean, we see that wave crests exist for a short period of time and then seems to disappear. This is because the crests we observe is composed of many wave components with different wave periods. As the long waves move faster than the short waves, the positive summation of components that formed the crest at a certain instant in time no longer exists after a short while. It should also be noted that the energy flux in the wave is slower than the wave celerity. The energy moves with a speed called the group velocity. In deep water, the group velocity is half the celerity.

The above equations summarize the key features of linear-gravity waves. From these equations, the velocities, accelerations etc. can be derived. Table 2.2 presents some key relations. Derivation of higher-order solutions, e.g., Stokes waves of orders two and five, may be found in Sarpkaya and Isaacson (1981) and Fenton (1985).

Table 2.2 gives an expression for the average energy density in the wave. This density is per unit free surface area. It can be shown that in deep water the average energy density has equally large contributions from the free surface elevation, the hydrostatic part and the kinematic part, i.e., the velocity squared term integrated from the bottom to the free surface. Note, however, that in wave energy applications, it is not the energy density per unit surface area that matters, but the energy flux in the direction of wave propagation. The energy flux per unit width of the wave crest is equal to the energy density multiplied by the group velocity of the waves.

The kinematics according to linear wave theory is valid for  $z \leq 0$  only. To estimate the kinematics above the mean water level, various approximations are used in practical applications. These are discussed in some detail in Section 2.2.7.

#### 2.2.4 Waves in Shallow Water

In deep water, the wave steepness is the only parameter important to the validity of the linear wave theory discussed here. In shallower water, the ratio of the water depth to the wavelength also becomes an important parameter. The following three parameters may be used to characterize waves in limited water depth (see DNV, 2014a).

Table 2.2 *Linear gravity on finite and infinite water depth.*  $\theta = (\omega t - kx \cos \chi - ky \sin \chi)$ , where  $\chi$  is direction of wave propagation relative to the positive  $x$ -axis;  $\zeta_A = H/2$  is the wave amplitude

Quantity	Finite water depth	Deep water
Potential	$\phi = i \frac{g}{\omega} \zeta_A \frac{\cosh[k(z+d)]}{\cosh(kd)} e^{i\theta}$	$\phi = i \frac{g}{\omega} \zeta_A e^{kz+i\theta}$
Surface elevation	$\zeta = \zeta_A e^{i\theta}$	$\zeta = \zeta_A e^{i\theta}$
Wave period $T = 2\pi/\omega$	$T = \frac{2\pi}{\sqrt{kg \tanh(kd)}}$	$T = \frac{2\pi}{\sqrt{kg}}$
Wavelength $\lambda = 2\pi/k$	$\lambda = cT = \frac{2\pi}{\omega} \sqrt{\frac{g}{k} \tanh(kd)}$	$\lambda = 2\pi \frac{g}{\omega^2}$
Phase velocity $c = \omega/k$	$c = \sqrt{\frac{g}{k} \tanh(kd)}$	$c = g/\omega$
Dynamic pressure	$p = -\rho \frac{\partial \phi}{\partial t} = \rho g \zeta_A \frac{\cosh[k(z+d)]}{\cosh(kd)} e^{i\theta}$	$p = \rho g \zeta_A e^{kz+i\theta}$
Particle velocity in $x$ -direction	$u_x = \frac{\partial \phi}{\partial x} = \frac{kg \cos \beta}{\omega} \zeta_A \frac{\cosh[k(z+d)]}{\cosh(kd)} e^{i\theta}$	$u_x = \omega \cos \beta \zeta_A e^{kz+i\theta}$
Particle velocity in $y$ -direction	$u_y = \frac{\partial \phi}{\partial y} = \frac{kg \sin \beta}{\omega} \zeta_A \frac{\cosh[k(z+d)]}{\cosh(kd)} e^{i\theta}$	$u_y = \omega \sin \beta \zeta_A e^{kz+i\theta}$
Particle velocity in $z$ -direction	$u_z = \frac{\partial \phi}{\partial z} = i \frac{kg}{\omega} \zeta_A \frac{\sinh[k(z+d)]}{\cosh(kd)} e^{i\theta}$	$u_z = i\omega \zeta_A e^{kz+i\theta}$
Particle acceleration in $x$ -direction	$a_x = \frac{\partial \phi}{\partial x \partial t} = ikg \cos \beta \zeta_A \frac{\cosh[k(z+d)]}{\cosh(kd)} e^{i\theta}$	$a_x = i\omega^2 \cos \beta \zeta_A e^{kz+i\theta}$
Particle acceleration in $y$ -direction	$a_y = \frac{\partial \phi}{\partial y \partial t} = ikg \sin \beta \zeta_A \frac{\cosh[k(z+d)]}{\cosh(kd)} e^{i\theta}$	$a_y = i\omega^2 \sin \beta \zeta_A e^{kz+i\theta}$
Particle acceleration in $z$ -direction	$a_z = \frac{\partial \phi}{\partial z \partial t} = -kg \zeta_A \frac{\sinh[k(z+d)]}{\cosh(kd)} e^{i\theta}$	$a_z = -\omega^2 \zeta_A e^{kz+i\theta}$
Group velocity	$c_g = \frac{1}{2} c \left( 1 + \frac{2kd}{\sinh(2kd)} \right)$	$c_g = c/2$
Average energy density	$E = \frac{1}{2} \rho g \zeta_A^2$	$E = \frac{1}{2} \rho g \zeta_A^2$
Average energy flux	$P = E c_g$	$P = E c_g = E \frac{c}{2}$

$$\begin{aligned}
 \text{Wave steepness parameter : } S &= \frac{H}{\lambda_0} = 2\pi \frac{H}{gT^2} \\
 \text{Shallow water parameter : } \mu &= \frac{d}{\lambda_0} = 2\pi \frac{d}{gT^2} \quad [2.53] \\
 \text{Ursell}^8 \text{ parameter : } U_r &= \frac{H}{k_0^2 d^3} = \frac{1}{4\pi^2} \frac{S}{\mu^3}
 \end{aligned}$$

Here,  $\lambda_0$  and  $k_0$  are the linear deep-water wavelength and wave number corresponding to the wave period  $T$ . The Ursell parameter expresses the ratio between the second-order amplitude and the first-order amplitude in a Stokes wave formulation (Sarpkaya and Isaacson, 1981) and is used to classify the range of validity for various wave descriptions. The Stokes second-order contribution to the surface elevation may be written as:

<sup>8</sup> The Ursell number is also written as  $U_R = 4\pi^2 U_r$  (DNV, 2021c).

$$\zeta^{(2)} = \frac{\pi H^2 \cosh(kd)}{8\lambda \sinh^3(kd)} [2 + \cosh(2kd)] e^{2i\theta}. \quad [2.54]$$

Here,  $H$  is the wave double amplitude, including both the first- and second-order contribution.

For the linear wave theory to be valid, the wave steepness should be small,  $S \ll 1$ . Further, the second-order component of the wave amplitude should be much less than the first-order amplitude. This is obtained if the Ursell parameter is much less than 1,  $U_r \ll 1$ . It is observed that if the shallow-water parameter,  $\mu$ , is reduced, then the Ursell parameter increases. This demonstrates that the Stokes wave representation of the waves breaks down in very shallow water.

The linear approach, also called Airy waves, has a fairly large range of validity with respect to wave steepness in deep water, while the range of validity is reduced as the water depth is reduced. Deep water may usually be assumed if  $\mu > 0.5$ . It is common to assume that the limiting steepness, or breaking limit, for regular waves in deep water is  $S=1/7$ . This is, however, far beyond the validity of linear theory. In very shallow water a breaking limit of  $H/d = 0.78$  is commonly assumed. For water that is not so shallow, the limit is lower (Grue et al., 2014).

Various recommendations exist with respect to the applicability of linear wave theory and various nonlinear formulations. Such recommendations may be found in various design standards, e.g., DNV (2021c). However, the applicability of the various approximations depends upon the use, e.g., if an accurate estimate of crest height is important, if local structural loads close to the free surface are to be estimated, if the loads are inertia- or drag-dominated etc.

From the above relations, it is observed that when waves move from deep water and into shallower water, the wavelength is shortened and the wave celerity slows down. As waves move from deep water, where they do not necessarily move perpendicular to the isobaths, into shallower water, the direction of the waves will change, tending to move perpendicular to the isobaths (see Figure 2.24). This phenomenon is called refraction. In Figure 2.24, we observe how the waves are directed away from deeper area focuses toward the shallower area. This causes wave energy to concentrate in the shallow area, increasing wave steepness. The refraction effect is strongest for long waves. If the coastline is not a shallow beach, but rather a steep cliff, waves will be reflected from the cliffs, causing a wave train that moves away from land. The combined refraction and reflection effects may thus cause very “confused” sea in the area. Details on wave refraction are found in Sarpkaya and Isaacson (1981).

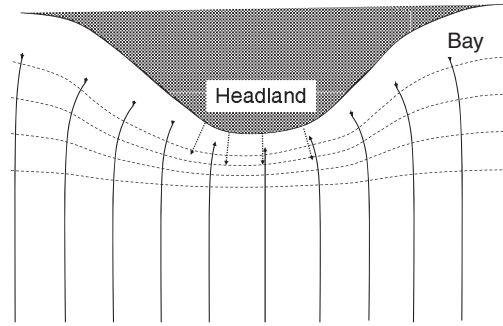


Figure 2.24 Refraction of waves approaching a shore. The dashed lines represent the isobaths (constant depth curves). The solid arrow represents the direction of wave propagation, while the dotted arrow indicates reflection from a steep headland. Based upon World Meteorological Organization (2018).

### 2.2.5 Energy in Waves

As in Table 2.2, the energy density per unit surface area for a linear-gravity wave is given by:

$$E = \frac{1}{2} \rho g \zeta_A^2. \tag{2.55}$$

This is independent of water depth and wave period. The energy is equally distributed between potential energy, given from the free surface elevation, and kinetic energy, given from the particle velocity throughout the water column.

The energy flux through a surface of unit width and perpendicular to the direction of wave propagation is given as:

$$P = c_g E. \tag{2.56}$$

$c_g$  is the group velocity of the waves. The group velocity may be illustrated by considering the summation of two regular waves of almost equal wave numbers,  $k$  and  $k + \delta k$ . The surface elevation is then given by:

$$\begin{aligned} \zeta(x, t) &= \zeta_{a1} e^{i(\omega(k)t - kx)} + \zeta_{a2} e^{i(\omega(k+\delta k)t - (k+\delta k)x)} \\ &\approx e^{i(\omega(k)t - kx)} \left[ \zeta_{a1} + \zeta_{a2} e^{i\left(\delta k \frac{\partial \omega}{\partial k} t - \delta k x\right)} \right]. \end{aligned} \tag{2.57}$$

Here, it is the real part of the expression that has physical meaning.  $\delta k$  represents the difference in wave number between the two waves. It is assumed that  $\delta k \ll k$ .  $\omega(k + \delta k)$  is the corresponding wave frequency. The last term in [2.57] represents a slowly oscillating term with frequency  $\delta k \frac{\partial \omega}{\partial k}$  and wave number  $\delta k$ . It is observed that the speed of this slowly oscillating term, the “group speed,” becomes:

$$c_g = \frac{\delta k \frac{\partial \omega}{\partial k}}{\delta k} = \frac{\partial \omega}{\partial k}. \tag{2.58}$$

Thus, the last term corresponds to a wave which propagates with the speed  $\partial \omega / \partial k$ . This is the speed of the “group” in the example shown in Figure 2.25. In the general case the group speed is obtained by derivation of the dispersion relation (see [2.49]):

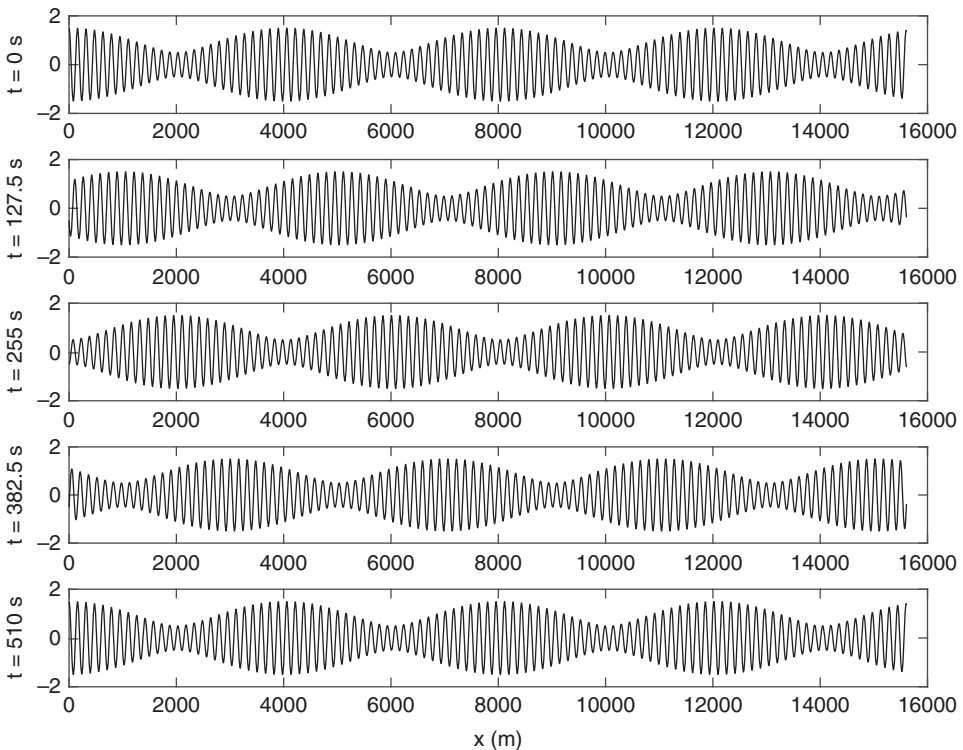


Figure 2.25 Example of summation of two waves of almost equal period ( $T = 10$  s and  $10.2$  s) in deep waters. The amplitudes are  $1$  and  $0.5$  m respectively. The group period becomes  $T_g = 1 / (1/T_1 - 1/T_2) = 510$  s. The plots are given at five equidistant time instants. The time interval between the plots is  $T_g/4$ . Each individual wave crest moves with a velocity  $c = \omega/g$ , about  $15.6$  m/s, while the peak of the group moves with a speed  $c_g = \omega/2g$ , about  $7.8$  m/s.

$$c_g = \frac{\partial}{\partial k} \sqrt{kg \tanh(kd)} = \frac{1}{2} \left( \frac{g}{k} \tanh(kd) \right)^{1/2} \left( 1 + kd \frac{1 - \tanh^2(kd)}{\tanh(kd)} \right). \quad [2.59]$$

Here, the relations  $\frac{d}{dx} \tanh(x) = \frac{1}{\cosh^2 x}$  and  $\cosh^2 x = \frac{1}{1 - \tanh^2 x}$  have been utilized. The expression for the group speed may be rewritten as:

$$c_g = \frac{1}{2} \left( \frac{g}{k} \tanh(kd) \right)^{1/2} \left( 1 + \frac{2kd}{\sinh(2kd)} \right) = \frac{1}{2} c \left( 1 + \frac{2kd}{\sinh(2kd)} \right), \quad [2.60]$$

where  $c$  is the phase speed of the wave; see [2.51].

The deep-water and shallow-water approximations for the group speed are obtained as:

$$c_{g(d \rightarrow \infty)} = \left. \frac{\partial \omega}{\partial k} \right|_{d \rightarrow \infty} = \frac{\partial}{\partial k} \sqrt{kg} = \frac{1}{2} \sqrt{\frac{g}{k}} = \frac{1}{2} \frac{g}{\omega} = \frac{1}{2} c_{(d \rightarrow \infty)} \quad [2.61]$$

$$c_{g(d \rightarrow 0)} = \left. \frac{\partial \omega}{\partial k} \right|_{d \rightarrow 0} = \frac{\partial}{\partial k} k \sqrt{gd} = \sqrt{gd} = c_{(d \rightarrow 0)}. \quad [2.62]$$

It is observed that in deep water, the group speed is half the phase velocity, while in the shallow water limit, the group and phase speeds are equal. Figure 2.25 illustrates how the sum of two deep-water waves of approximately the same period propagates. It is observed that the peak of the group moves with half the phase speed, as derived in [2.61].

An example of the group speed as a function of water depth is given in Figure 2.26. The general picture is that the group speed is reduced as the water depth is reduced. However, in a range where the water depth is about 0.15–0.2 times the wavelength, the group speed increases.

Consider waves moving from deep water toward shallow water. The energy flux through every cross-section perpendicular to the direction of wave propagation must be constant; i.e., according to [2.56], it is obtained that the wave height has to vary as  $H(d)/H_{d \rightarrow \infty} = \sqrt{c_{g(d \rightarrow \infty)}/c_g(d)}$ . The resulting wave height is shown in Figure 2.26, together with the shallow-water approximation.

### 2.2.6 Superposition of Waves: Wave Spectrum

A real sea state cannot be modeled as a regular wave. Sometimes swells may almost resemble a regular wave with constant period and amplitude. However, under the assumption of linearity, wind-generated gravity waves may be modeled as a summation of regular waves with different wave periods and

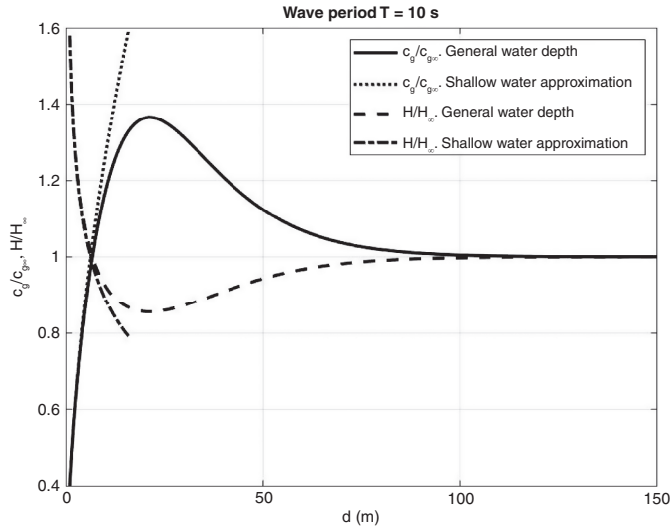


Figure 2.26 Group speed and wave height for a 10 s wave as a function of water depth. The group speed and wave height are normalized with the deep-water values.

amplitudes; i.e., assuming unidirectional waves, the wave elevation may be written as:

$$\zeta(t, x) = \text{Re} \left\{ \sum_{j=1}^N A_j e^{i(\omega_j t - k_j x + \phi_j)} \right\} = \sum_{j=1}^N A_j \cos(\omega_j t - k_j x + \phi_j). \quad [2.63]$$

Here,  $A_j$  is the wave amplitude of wave component  $j$  with corresponding wave number  $k_j$  and angular frequency  $\omega_j$ .  $\phi_j$  is the phase of component  $j$ . If  $N \rightarrow \infty$ , the wave field may be described by a continuous wave spectrum, or a wave energy spectrum. In the description of ocean waves, a one-sided spectrum is most commonly used, i.e., the spectrum is given for positive frequencies only. Examples of such spectra are given in Figure 2.27. The wave energy spectrum contains information of the amplitudes of the wave components, or rather the energy, as a function of wave frequency. Information of the phase is not present. If the continuous spectrum is divided into finite frequency intervals,  $\Delta\omega = 2\pi\Delta f$ , the amplitude of the wave component corresponding to a specific interval is given by:<sup>9</sup>

<sup>9</sup> Note that  $S(f) = 2\pi S(\omega)$ , so  $S(f)\Delta f = S(\omega)\Delta\omega$ .

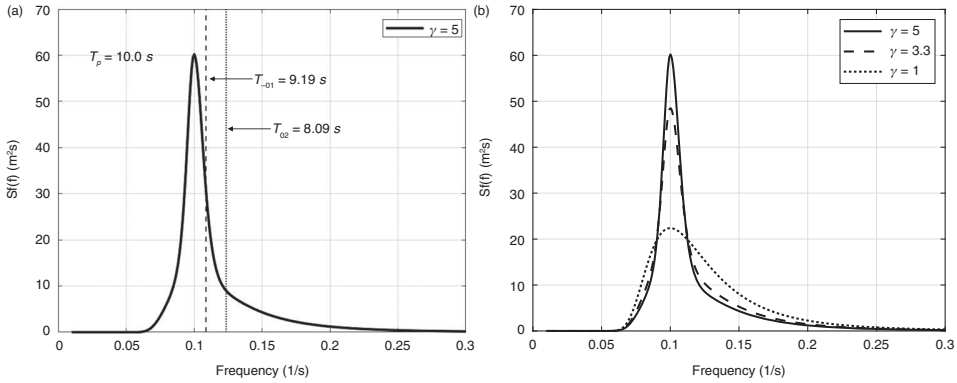


Figure 2.27 The Jonswap wave spectrum. Left: example on a spectrum with  $H_s = 5.0\text{ m}$  and  $T_p = 10\text{ s}$ . Right: spectra with different  $\gamma$  values.  $H_s = 5\text{ m}$  and  $T_p = 10\text{ s}$ .

$$A_j = \sqrt{2S(\omega_j)\Delta\omega_j}. \tag{2.64}$$

This means that the area of the spectrum over this frequency interval is proportional to the energy in a corresponding regular wave component. The wave spectrum may be obtained from measurements, by taking the Fourier transform of the measured wave elevation at a specific point in the sea. For design purposes several standard spectra exist. These are developed to be representative of typical average sea states. Two frequently used spectral representations of ocean waves are the Pierson–Moskowitz (PM) spectrum and the Jonswap spectrum. According to DNV (2021c) the PM spectrum may be written as:

$$S_{PM}(\omega) = \frac{5}{16}H_s \frac{\omega_p^4}{\omega^5} e^{\left[-\frac{5}{4}\left(\frac{\omega}{\omega_p}\right)^{-4}\right]}. \tag{2.65}$$

Here,  $H_s$  is the significant wave height. Traditionally this corresponded to the visually observed wave height but now has a more stringent definition related to the energy in the sea state or the area of the wave spectrum (see text following [2.67]). Sometimes, the significant wave height has also been directly related to the time history of the wave record and denoted  $H_{1/3}$ , which is the average of the 1/3 highest waves (double amplitudes) in the sea state (World Meteorological Organization, 2018).  $\omega_p = 2\pi/T_p$  is the peak angular frequency of the spectrum with corresponding period  $T_p$  (see Figure 2.27). A wave spectrum is defined for a



stationary wave condition, a hypothetical situation where all parameters as well as the shape of the spectrum are constant over time. As sea states are always changing as a response to the weather, a truly stationary sea state cannot exist. However, for design purposes, one normally considers a sea state to be stationary for 3 h. The PM spectrum is considered a reasonable description of a fully developed sea state, i.e., when the wind has been blowing for a long time with constant strength and direction over a large sea area (fetch). A more realistic assumption is that the sea is under development and that the fetch is limited. For such cases the Jonswap spectrum is a reasonable description. The Jonswap spectrum is an  $\gamma$ -adjusted version of the PM spectrum:

$$S_J(\omega) = A_\gamma S_{PM}(\omega) \gamma^{\exp\left[-0.5\left(\frac{\omega-\omega_p}{\sigma\omega_p}\right)^2\right]} \quad [2.66]$$

Here,  $\gamma$  is a nondimensional peak shape parameter;  $\sigma$  is a spectral width parameter with  $\sigma = \sigma_a$  for  $\omega \leq \omega_p$  and  $\sigma = \sigma_b$  for  $\omega > \omega_p$ ;  $A_\gamma = 1 - 0.287\ln(\gamma)$  is a normalizing factor. Normally  $\sigma_a = 0.07$  and  $\sigma_b = 0.09$  are used. An average value of  $\gamma$  is 3.3; however, values in the range  $\gamma = [1, 5]$  may be encountered.  $\gamma = 1$  corresponds to the PM spectrum. In Figure 2.27 (right), a Jonswap spectrum is illustrated using different  $\gamma$ -values.

Given a wave spectrum  $S(\omega)$ , various parameters may be defined. The  $n^{\text{th}}$  spectral moment is defined by:

$$m_n = \int_0^\infty \omega^n S(\omega) d\omega. \quad [2.67]$$

The significant wave height is then defined by  $H_s = 4\sqrt{m_0}$ .  $m_0$  is equal to the square of the standard deviation of the surface elevation. For a “narrow-banded” spectrum the average zero up-crossing period is obtained as  $T_{02} = 2\pi\sqrt{m_0/m_2}$ . In Figure 2.27 (left), a Jonswap spectrum with  $H_s = 5.0$  m is illustrated. Here, the peak frequency  $f_p = 1/T_p$  as well as the zero up-crossing frequency  $f_{02} = 1/T_{02}$  and energy mean frequency  $f_{-01} = m_0/(2\pi m_{-1}) = 1/T_{-01}$  are shown. The energy mean period is the period of a regular wave with the same flux of energy as the mean flux of energy in the the wave spectrum, assuming deep water.

The term “narrow-banded” can be understood in the sense that the wave elevation record, and thus the wave spectrum, is narrow-banded if there is only one maximum or minimum value (wave crest or wave trough) between every crossing of the average value. On the contrary, a broad-banded process has several maxima and minima between every crossing to the average value.

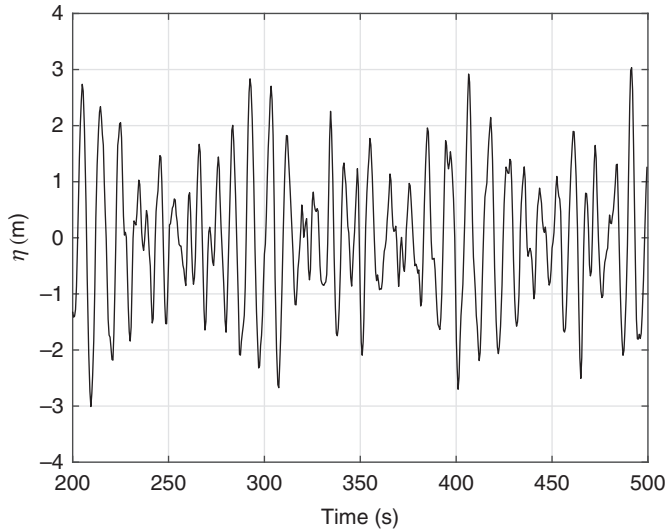


Figure 2.28 Example of a realization of a time history of a Jonswap spectrum with  $H_s = 5.0$  m,  $T_p = 10.0$  s and  $\gamma = 5$ .  $T_{02} = 8.1$  s.

This is the case when small, short waves ride on top of long, large waves. Figure 2.28 shows an example of a realization of the wave spectrum in Figure 2.27 (left). The time history is obtained by using a fast Fourier transform of the wave spectrum, using about 1000 frequency components with random phases in the range 0 – 2 Hz. It is observed that the “narrow-band” criterion of only one extremum between each zero-crossing is almost fulfilled. To illustrate a broad-banded process, the rectangular spectrum in Figure 2.29 is used. A realization of a time history based upon this spectrum is shown in Figure 2.30. Here, several extreme values are observed between each zero-crossing. More details on spectral formulation and stochastic processes may be found in, e.g., Naess and Moan (2013).

In the above description of the waves, it is assumed that all wave components are progressing in the same direction. However, within the framework of linearity, a summation of wave components progressing in different directions works as well. We then obtain so-called “short-crested” waves. A common way of writing the directional wave spectrum is by introducing a directional weight function, i.e., the wave spectrum is written as:

$$S(\omega, \chi) = S(\omega)D(\chi). \quad [2.68]$$

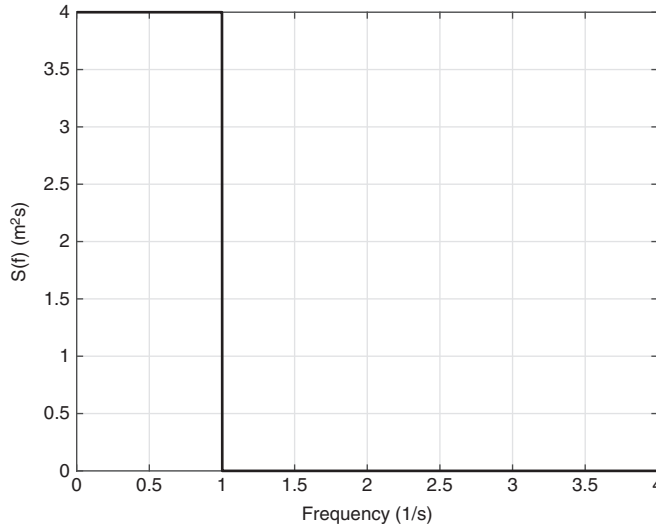


Figure 2.29 Rectangular, broad-banded spectrum with area equal to  $4 \text{ m}^2$ .

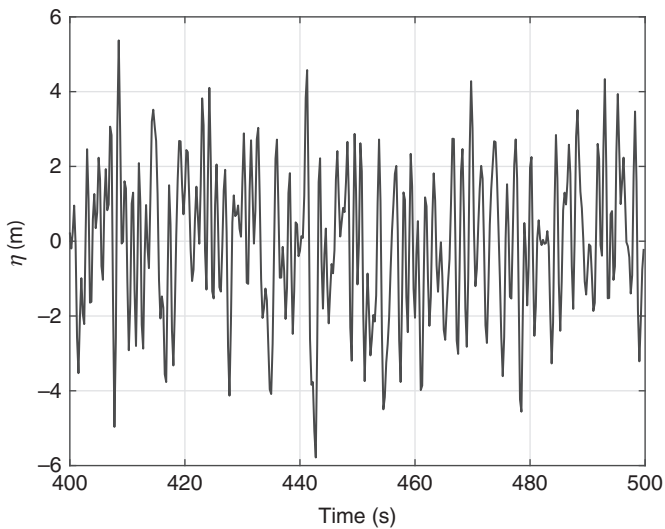


Figure 2.30 Extract of a realization of a time history of the spectrum in Figure 2.29.

Here,  $D(\chi)$  is the directional weight factor, which has the property  $\int_{\theta} D(\chi) d\chi = 1$ . The integral is to be taken over all wave directions. A commonly used directional function (see DNV, 2021c) is:

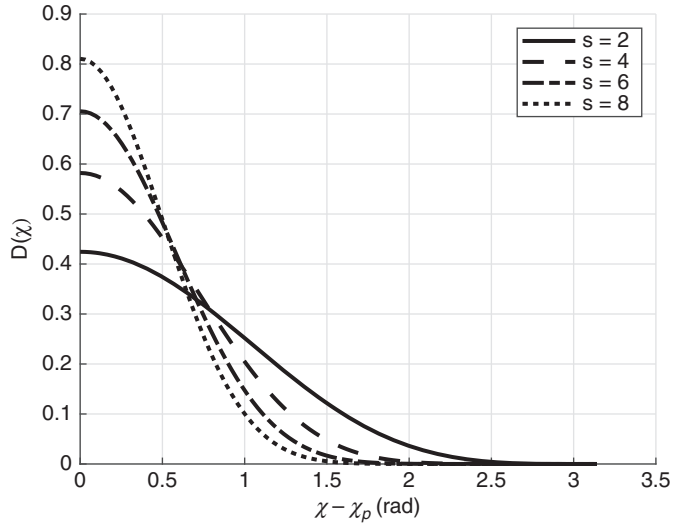


Figure 2.31 The directional spreading function,  $D(\chi)$ , for different values of  $s$ .

$$D(\chi) = \frac{\Gamma(s+1)}{2\sqrt{\pi} \Gamma(s+1/2)} \cos^{2s} \left( \frac{1}{2} (\chi - \chi_p) \right). \quad [2.69]$$

Here, the first term contains Gamma-functions, which are present to secure that the integral over all directions becomes unity.  $\chi_p$  is the prevailing wave direction and  $|\chi - \chi_p| \leq \pi$ . For wind sea, typical values of  $s$  are in the range 5–15, while swells may have  $s > 15$ . Examples of the directional spreading function are shown in Figure 2.31. In the above formulation of the directional spreading, all wave components get the same directional spreading. This is normally not the case in real seas. Thus, a more realistic formulation is to introduce frequency-dependent spreading, i.e.,  $D = D(\chi, \omega)$ . To find a proper function suitable for design is, however, a challenge.

### 2.2.7 Wave Kinematics in Irregular Waves

When estimating wave kinematics, particle velocities and accelerations, in an irregular sea, we may as a first approximation use linear superposition, as for the wave elevation. This works well below the mean free surface level. However, above the mean free surface level we have a challenge as linear theory is not valid here. Several engineering approaches exist for how to estimate the wave kinematics in wave crests. It is of particular importance to have good estimates on the velocities in the water under the highest wave crests. These velocities may in many cases determine the extreme loads on marine structures. Thus, to obtain

reliable designs, reliable velocity estimates are of vital importance. The following three methods are frequently used for estimating kinematics in wave crests (NORSOK, 2017).

- Wheeler stretching
- Second-order kinematic models
- CFD techniques

Which method to use depends upon the accuracy required in the estimates as well as the design conditions to be considered. Wheeler stretching is frequently used in engineering applications as the method is simple and it is straightforward to implement. The method is based on the assumption that a wave elevation record is available, e.g., from measurements. The idea is to use the sum of the linear velocities from each spectral component, “re-computed” using a water depth from the actual free surface  $d' = d + \zeta$ . The computed velocities are assumed valid from the actual free surface level downwards. The principle is illustrated in Figure 2.32. Using direct extrapolation of the linear velocity profile above the mean surface level will usually overestimate the fluid velocities, in particular for the short wave components. In steep waves the Wheeler stretching method may underestimate the fluid velocities.

More consistent methods based upon second-order perturbations have been developed; see, e.g., Stansberg (2011) and Johannessen (2011). Birknes et al. (2013) have compared various approaches. In general, all such perturbation approaches tend to fail for very steep waves. Methods based upon second-order perturbations also have limited applicability in shallow water. Thus, for very steep waves and shallow water, methods using computational fluid dynamics (CFD) techniques or model testing seem to be the most appropriate approaches to obtain proper wave kinematics. However, to study the local kinematics in steep, breaking waves, methods based upon potential theory have also been developed. For

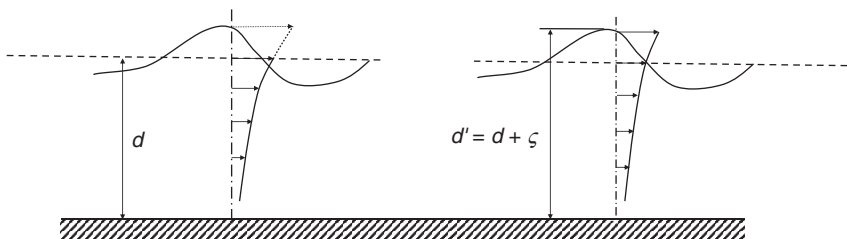


Figure 2.32 Illustration of Wheeler stretching versus pure extrapolation. Left: velocity profile under wave crest, extrapolated linear profile indicated by dotted line. Right: Wheeler stretching.

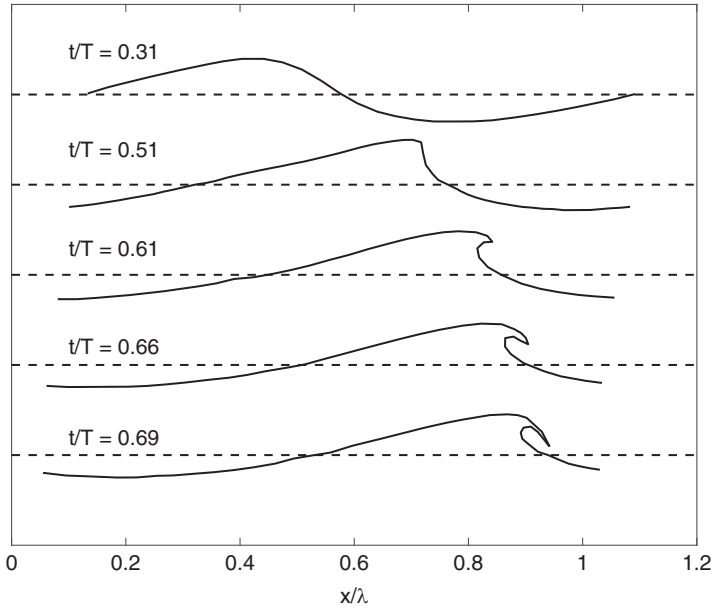


Figure 2.33 Wave profile of a plunging breaker in deep water;  $T$  is the wave period. The initial state is a steep sinusoidal wave. As computed by Vinje and Brevig (1980). Reproduced with permission by SINTEF OCEAN.

example, Vinje and Brevik (1980) developed a boundary element method based upon potential theory to compute the development of steep, breaking waves. The method assumes a train of equal waves and breaks down when the wave crest hits the free surface. Results from the method are illustrated in Figure 2.33. The computations indicate maximum fluid velocities in the crest beyond the phase velocity of the wave and accelerations in excess of the acceleration due to gravity.

### 2.3 Wave Statistics

In wave statistics a distinction is made between short- and long-term statistics. Short-term statistics assumes a stationary sea state, i.e., all statistical parameters are constant in the period considered. The process is also assumed to be ergodic. In ocean wave applications the definition of “short-term” frequently is in the range of 1–3 h. The period chosen is often a compromise between the stationarity of the sea state and the require length to achieve proper response statistics of the structure considered.

Long-term statistics considers the statistics of key parameters as significant wave height and mean zero-crossing period over time intervals of month to many years.

### 2.3.1 Short-Term Statistics

During a short period of time, the wave condition may be considered stationary. Assuming stationarity, adhering to the linearity assumption and assuming a narrow-banded process, some simple statistics may be derived for the wave heights. We may assume that the surface elevation is represented by a Gaussian process. The statistics of wave heights (trough to crest) may then be modeled by a Rayleigh distribution, see Figure 2.34, i.e.:

$$P_H(h) = 1 - e \left[ - \left( \frac{h}{\alpha_H H_s} \right)^2 \right]. \quad [2.70]$$

Here,  $P_H(h)$  is the cumulative probability of the wave height, being less than  $h$ .  $\alpha_H$  is a parameter related to the spectral width, for an infinitely narrow-band process  $\alpha_H = \frac{1}{2}\sqrt{2}$ . Næss (1985) found that for real sea states,  $\alpha_H$  could be expressed by  $\alpha_H = \frac{1}{2}\sqrt{1 - \rho}$ .  $\rho$  is related to the bandwidth of the wave spectrum. For a Jonswap spectrum with  $\gamma = 3.3$  the value of  $\rho$  is obtained as  $-0.73$  (DNV, 2021c). Næss (1985) finds that for most sea states with some severity and without significant swell,  $-0.75 < \rho < -0.65$ ; see Næss and Moan (2013).

During a period of time  $t$  (e.g., 3 h), the number of waves passing a fixed point is  $N = t/T_{02}$ . If the random process is repeated many times, and assuming a narrow-banded Rayleigh distribution, the mean values of the maxima in each of the repeated records will tend toward :

$$H_{\max,mean} = \left[ \sqrt{\frac{1}{2} \ln N} + \frac{0.2886}{\sqrt{2 \ln N}} \right] H_s. \quad [2.71]$$

The most probable highest wave in a realization (the mode) is similarly given by:

$$H_{\max,mod} = \left[ \sqrt{\frac{1}{2} \ln N} \right] H_s. \quad [2.72]$$

Thus, if we have a wave condition with zero up-crossing period  $T_{02} = 10\text{ s}$ , then 1080 waves will pass during a period of 3 h. The most probably largest wave during a realization will then be  $1.87H_s$ , while the average maximum wave during several realizations will be  $1.95H_s$ . Care should be shown in using the Rayleigh distribution in shallow water. Here, the wave height will typically be limited to 0.78 times the water depth and the tail of the distribution will be distorted. Alternative distributions for the wave heights exists for shallow water; see, e.g., DNV (2021c).

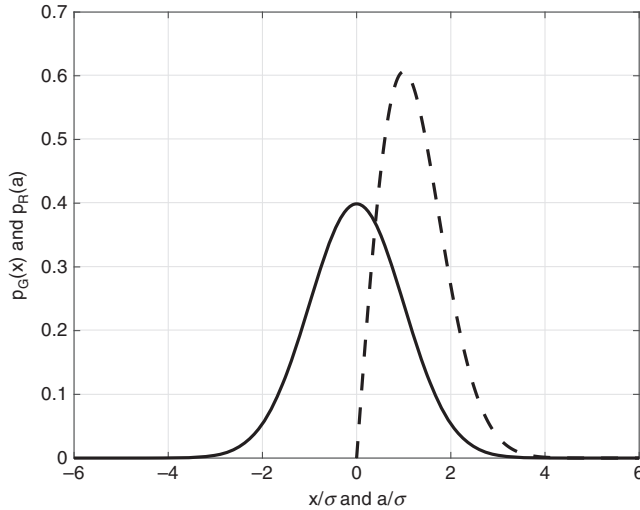


Figure 2.34 Illustration of the probability distribution of a Gaussian free surface elevation  $x$  (solid line) and the corresponding Rayleigh distribution of the amplitudes  $a$  (dashed line) for a narrow-band process with  $\alpha_H = 0.5\sqrt{2}$ .

For many applications it is more important to have a good estimate of the extreme crest height rather than the wave height. The Forristall distribution may be used for that purpose (DNV 2021c).

### 2.3.1.1 Confidence Limits for Short-Term Extreme Values

In analyzing wave time series, very often the extreme value is of interest. It is therefore of interest to estimate the confidence limit of an extreme value obtained from a single realization of a process, either by measurement or simulation. This can be done as follows.

Assume a narrow-band process,  $x(t)$ , with zero mean, i.e., there is only one positive peak between every zero up-crossing. The peaks are denoted  $x_a$  and are assumed independent, i.e., there is no correlation between two neighboring peaks. The cumulative distribution of peaks is denoted  $P(\xi) = \text{prob}(x_a < \xi)$ . As the peaks are assumed independent, the probability of having  $N$  peaks less than  $\xi$  is given by:

$$\text{prob}(x_{a1}, x_{a2}, \dots, x_{aN} < \xi) = [P(\xi)]^N. \quad [2.73]$$

The desired confidence limits are the positive and negative extreme values given by:



$$[P(\xi)]^N = \begin{cases} 1 - \varepsilon \\ \varepsilon \end{cases}, \tag{2.74}$$

where  $\varepsilon \ll 1$  is assumed. Assume further that the amplitudes are Rayleigh-distributed with probability density and cumulative probability given by:

$$\begin{aligned} p(\xi) &= \frac{\xi}{\sigma_x^2} e^{-\frac{\xi^2}{2\sigma^2}} \\ P(\xi) &= 1 - e^{-\frac{\xi^2}{2\sigma^2}} \end{aligned} \tag{2.75}$$

To establish the probability that the extreme value for a realization of the process stays within the interval given by [2.74], one has to compute  $\alpha_1 = P(\xi_1) = \varepsilon^{1/N}$  and  $\alpha_2 = P(\xi_2) = (1 - \varepsilon)^{1/N}$ . Inserting for the Rayleigh distribution, the following is obtained:

$$\begin{aligned} P(\xi) &= 1 - e^{-\frac{\xi^2}{2\sigma^2}} = \alpha \\ \frac{\xi}{\sigma} &= \sqrt{-2\ln(1 - \alpha)} \end{aligned} \tag{2.76}$$

**Confidence Limits for Maximum Values**

*Assume the amplitude distribution obeys the Rayleigh distribution. Set  $\varepsilon = 0.05$  and assume the number of oscillations to be  $N = 200$ . The  $100(1 - 2\varepsilon) = 90$ -percentile interval is thus given from the probability levels:*

$$\begin{aligned} P(\xi_1) &= \varepsilon^{1/N} = 0.05^{1/200} = 0.98510 = \alpha_1 \\ P(\xi_2) &= (1 - \varepsilon)^{1/N} = 0.95^{1/200} = 0.9974 = \alpha_2 \end{aligned}$$

*Inserting into [2.76] the lower and upper limit for the 90th-percentile interval is found as*

$$\frac{\xi_1}{\sigma} = 2.90, \quad \frac{\xi_2}{\sigma} = 4.07,$$

*while the most probable extreme value in a Rayleigh distribution is given from  $\frac{x_{\max, \text{mod}}}{\sigma} = \sqrt{2\ln N} = 3.26$ .*

Some nonlinear response processes induced by, for example, slow-drift wave loads or low-frequency wind forces may have a statistic of peaks that significantly

deviates from the Rayleigh distribution. Sometimes the response statistics are closer to an exponential distribution, i.e.:

$$P(\xi) = 1 - e^{-\frac{\xi}{\sigma}}. \tag{2.77}$$

Following the procedure above, the confidence limit for the exponential distribution is found from:

$$\frac{\xi}{\sigma} = -\ln(1 - \alpha). \tag{2.78}$$

In Figure 2.35, the most probable maximum amplitudes and the corresponding 90th-percentile interval for a Rayleigh and an exponential distribution are shown. It is clearly observed that the exponential process has higher expected extreme values as well as a larger confidence interval.

### 2.3.2 Long-Term Wave Statistics

Assume that during a long period of time, say, one year, the wave conditions may be described by a large number of stationary wave conditions of duration, for example, of 3 h. Each of these stationary conditions may be characterized by key spectral parameters such as significant wave height and spectral peak period. Each of the 3 h periods are assumed independent. In an average year, there will be 2922 such

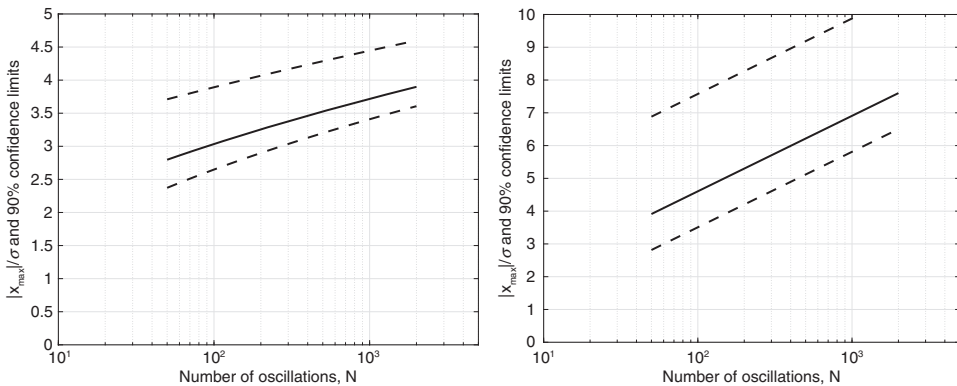


Figure 2.35 Most probable largest value in a narrow-banded process with Rayleigh-distributed (left) and exponential-distributed (right) amplitudes as a function of number of oscillations. Solid line: most probable value. Dashed lines: lower and upper limits for the 90th-percentile interval. Zero mean value is assumed.

periods. To present the long-term statistics of the key wave parameters, a “scatter diagram” is frequently used, as illustrated in Table 2.4. The data are based upon approximately 18 years of measured data, altogether 52 365 wave records. The measured significant wave heights are grouped in bins of 0.5 m and the peak periods are grouped in bins of 1 s. The numbers given in the scatter diagram are the number of observations within each  $H_s - T_p$  bin combination. The marginal and cumulative probability with respect to  $H_s$  and  $T_p$  are given along the edges of the table. For these specific data the yearly average  $H_s$  is obtained as 2.77 m and the yearly average  $T_p$  is 9.52 s. It is also observed that the most probable value (the mode) of the significant wave height and the peak period are both lower than the corresponding average values. This illustrates the skewness in the probability distributions. The scatter diagram in Table 2.4 includes all wave directions. For design purposes, such diagrams are frequently made for several wave directions, typically 12 wave sectors, each of 30 deg.

In the design of marine structures, extreme value estimates are needed. This may be either the extreme wave height independent of spectral peak period or the extreme wave height given a spectral peak period.

For the long-term distribution of the significant wave height, a three-parameter Weibull distribution may be used. The cumulative probability using the three-parameter Weibull distribution may be written in the form:

$$P_{H_s}(h) = 1 - \exp \left[ - \left( \frac{h - \gamma}{\alpha} \right)^\beta \right]. \tag{2.79}$$

$\alpha (> 0)$  is the scale parameter, used to normalize the variable;  $\gamma (\leq h)$  is the location parameter, used to define a lower threshold for the variable; and  $\beta (> 0)$  is the shape parameter, defining the shape of the distribution. Consider periods of duration of 3 h. If we want to estimate the significant wave height that is exceeded once every  $N^{\text{th}}$  year, the probability level we are seeking, the target probability, is given by:

$$P_N = \left( \frac{24}{3} \cdot 365.25 \cdot N \right)^{-1} = N_i^{-1}. \tag{2.80}$$

Here, the first factor is the number of 3 h data points per day and 365.25 is the average number of days per year. Using the three-parameter Weibull distribution, the significant wave height that is expected to on average be exceeded once every  $N^{\text{th}}$  year is now given by:

$$H_{sN} = \gamma + \alpha \left( \ln(N_i) \right)^{1/\beta}. \tag{2.81}$$

In estimating the parameters in the Weibull distribution, all the available data are used. However, it is frequently observed that the tail of the distribution, representing the highest waves, deviates slightly from the distribution obtained using the complete dataset. Therefore, in estimating the extreme value for a long period of time, e.g., 50 years, two other methods are frequently employed: the annual maximum (AM) method and the peak over threshold (POT) method.

In the AM method, only the largest significant wave height measured every year is used in the statistical distribution. The data are fitted to a Gumbel distribution in the form:

$$P_{H_{se}}(h_e) = \exp\left(-\exp\left(-\frac{h_e - \mu}{\sigma}\right)\right). \quad [2.82]$$

Here,  $h_e$  is the distribution of the yearly extreme significant wave height;  $\mu$  is the location parameter; and  $\sigma$  is the scale parameter. The significant wave height expected to be exceeded once every  $N^{\text{th}}$  year is now given by:

$$H_{sN} = \mu - \sigma \left[ \ln\left(-\ln\left(1 - \frac{1}{N}\right)\right) \right]. \quad [2.83]$$

To obtain a reliable extreme value estimate by the AM method, data for many years are needed.

The POT method represents an alternative. Here, all measured significant wave heights above a certain threshold are used to establish the extreme value distribution. Thus, many values per year may enter the distribution without accounting for all the small  $H_s$ . A basic assumption in this approach is that all  $H_s$  entering the distribution are independent, i.e., they do not belong to the same storm event. A key issue related to the POT method is the choice of threshold. The choice of an excessively high threshold leads to few data entering into the distribution, causing greater uncertainty in the estimates than for the AM method. Choosing a threshold that is too low leads to a lot of low wave heights entering the distribution, introducing a possible bias to the extremes, in the same way as for the Weibull approach.

Details related to the use of the methods are found in, for example, Orimolade et al. (2016) and Naess and Moan (2013).

In Figures 2.36 and 2.37, the significant wave heights in the northern North Sea from measurements over a period of about 18 years are presented. The measurements are taken once every third hour. The stars are the distribution based upon binned data. 100 bins are used. The solid line is the fitted three-parameter Weibull distribution. The logarithmic scaling in Figure 2.37 is introduced to obtain a linear

relation between the two axes for large  $H_s$  values. By this scaling it is also possible to read out the wave heights corresponding to low probability of exceedance.

### Long-Term Extreme Value

Find an estimate on the 3 h significant wave height expected to be exceeded once every  $N^{\text{th}}$  year. The aim is thus to find a wave height with probability of exceedance equal to  $1/(N \cdot 8760/3)$ . The significant wave height that is expected to be exceeded once during a period of 50 years corresponds to cumulative probability level of  $H_s$  equal to  $1 - 1/146000$ . On the Weibull scale this becomes  $\ln(-\ln(1/146000)) = 2.4758$ . Using [2.81] and the distribution fitted to the data in Figure 2.36, the corresponding 50-year extreme 3 h significant wave height becomes:

$$H_{s50} = 0.6234 + 2.370 \cdot \left( \ln(146000) \right)^{1/1.425} = 14.09\text{m}. \quad [2.84]$$

Similar results for 1–100-year extreme values are shown in Table 2.3.

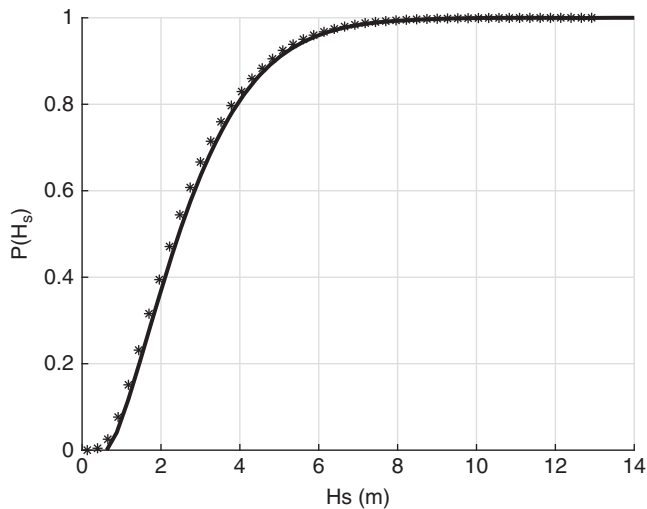


Figure 2.36 The cumulative probability of significant wave height. The stars are binned measured data over a period of approximately 18 years from the northern North Sea. The solid line is a fitted three-parameter Weibull distribution with  $\alpha = 2.370$ ,  $\beta = 1.425$  and  $\gamma = 0.6234$ .

Table 2.3 Example of expected 3 h extreme significant wave height versus return period using the Weibull distribution obtained by fitting the data in Figure 2.36

Return Period, N (years)	Probability Level	
	$\ln(-\ln(1/2920 \cdot N))$	3 h extreme $H_s$ (m)
1	2.0769	10.80
10	2.3304	12.78
50	2.4758	14.09
100	2.5325	14.64

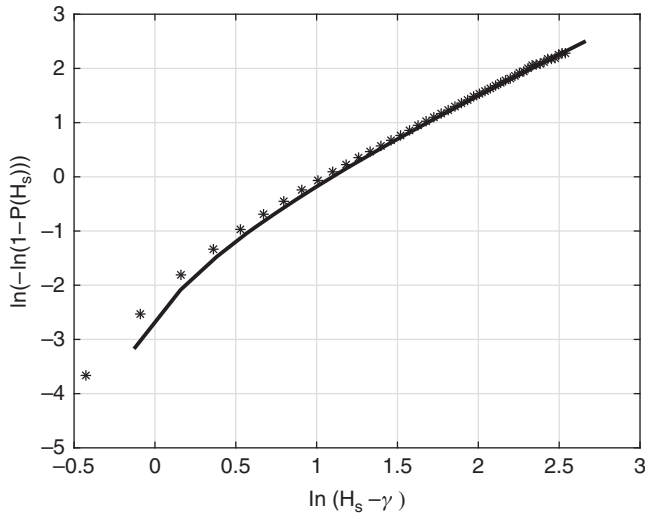


Figure 2.37 As Figure 2.36, but plotted on a Weibull scale.

## Exercises Chapter 2

1. Which main assumptions are used to derive the logarithmic vertical profile for the mean wind velocity?
2. In engineering applications an exponential wind profile is frequently used rather than a logarithmic profile. Assume the wind speed at 10 m above sea level is known. Compute the wind profile by the logarithmic and the exponential approach in the range 1–250 m above sea level. Discuss how the two profiles deviate. How will the profiles match if you force the velocities to be equal at a higher level than at the reference level of 10 m?

Table 2.4 Scatter diagram. Example based upon approximately 18 years of measured data from the North Sea.

Hs (m)	<4	4-5	5-6	6-7	7-8	8-9	9-10	10-11	11-12	12-13	13-14	14-15	15-16	16-17	17-18	18-19	19-20	>=20	Merg prob	Cum prob
<0.5	25	14	18	14	24	17	8	9	5	0	2	3	1	1	6	2	0	7	156	0.0030
0.5-1	79	225	408	539	496	488	426	225	111	46	16	7	6	3	2	0	2	17	3106	0.0623
1-1.5	71	466	896	1223	1227	1219	911	626	470	252	108	70	36	12	13	2	4	49	7653	0.1461
1.5-2	3	134	768	1342	1443	1288	1143	864	618	404	205	129	44	21	10	3	4	21	8434	0.1611
2-2.5	0	22	292	1013	1328	1359	1056	921	669	431	188	186	56	27	17	5	1	16	7587	0.1449
2.5-3	1	2	79	491	1037	1276	1031	795	678	479	208	193	81	35	13	3	2	8	6412	0.1224
3-3.5	0	1	16	189	701	1038	896	729	532	386	235	197	97	40	15	4	1	5	5082	0.0970
3.5-4	0	0	3	57	318	814	767	562	447	371	193	168	89	50	17	3	0	3	3862	0.0738
4-4.5	1	0	1	11	130	568	731	500	341	306	146	142	67	29	25	4	3	2	3007	0.0574
4.5-5	0	0	0	3	44	329	533	444	337	248	122	95	40	31	20	2	4	1	2253	0.0430
5-5.5	0	0	0	1	15	112	339	396	280	195	121	98	31	26	16	5	2	0	1637	0.0313
5.5-6	0	0	0	1	4	46	193	244	177	138	73	70	27	15	15	3	0	1	1054	0.0201
6-6.5	0	0	0	0	1	18	91	177	156	125	65	51	20	15	7	1	2	2	730	0.0139
6.5-7	0	0	0	0	1	34	108	137	106	46	40	40	14	5	1	2	0	0	495	0.0095
7-7.5	0	0	0	0	1	1	11	53	93	74	50	30	14	7	8	0	1	0	342	0.0065
7.5-8	0	0	0	0	0	1	29	61	63	27	19	6	3	1	1	1	0	1	212	0.0040
8-8.5	0	0	0	0	0	1	0	14	31	43	24	13	6	5	1	0	0	0	138	0.0026
8.5-9	0	0	0	0	0	0	0	8	19	27	17	8	7	1	0	0	0	0	87	0.0017
9-9.5	0	0	0	0	0	0	0	2	5	18	13	9	2	1	1	0	0	0	51	0.0010
9.5-10	0	0	0	0	0	0	0	1	2	7	7	4	3	3	0	0	0	0	27	0.0005
10-10.5	0	0	0	0	0	0	0	1	3	3	7	4	4	1	0	0	0	0	22	0.0004
10.5-11	0	0	0	0	0	0	0	0	3	3	1	2	0	0	0	0	0	0	6	0.0001
11-11.5	0	0	0	0	0	0	0	0	4	2	1	0	0	0	0	0	0	0	7	0.0001
11.5-12	0	0	0	0	0	0	0	0	0	1	0	0	0	0	0	0	0	0	1	0.0000
12-12.5	0	0	0	0	0	0	0	0	0	1	0	0	1	0	0	0	0	0	2	0.0000
12.5-13	0	0	0	0	0	0	0	0	0	0	0	0	0	0	1	0	0	0	1	0.0000
13-13.5	0	0	0	0	0	0	0	0	0	0	1	0	0	0	0	0	0	0	1	0.0000
13.5-14	0	0	0	0	0	0	0	0	0	0	0	0	0	0	0	0	0	0	0	0.0000
14-14.5	0	0	0	0	0	0	0	0	0	0	0	0	0	0	0	0	0	0	0	0.0000
14.5-15	0	0	0	0	0	0	0	0	0	0	0	0	0	0	0	0	0	0	0	0.0000
>=15	0	0	0	0	0	0	0	0	0	0	0	0	0	0	0	0	0	0	0	0.0000
Merg sum	180	874	2481	4884	6768	8575	8171	6697	5219	3731	1877	1539	652	331	189	40	24	133		
Cum sum	180	1054	3535	8419	15187	23762	31933	38630	43849	47580	49457	50996	51648	51979	52168	52208	52232	52365		
Merg prob	0.0034	0.0167	0.0474	0.0933	0.1292	0.1638	0.1960	0.1279	0.0997	0.0712	0.0358	0.0294	0.0125	0.0063	0.0036	0.0008	0.0005	0.0025		
Cum prob	0.0034	0.0201	0.0675	0.1608	0.2900	0.4538	0.6098	0.7377	0.8374	0.9086	0.9445	0.9739	0.9863	0.9926	0.9962	0.9970	0.9975	1.0000		

3. [2.11] gives the flux Richardson number. A gradient Richardson number may be written as  $R_g = \frac{g\bar{\theta}'\bar{w}'}{(\bar{u}')^2}$ . Show that  $R_g/R = K_m/K_h$ , where  $K_m$  and  $K_h$  are the eddy diffusivity for momentum and heat respectively.
4. Turbulence is frequently described as a stationary, Gaussian, homogeneous and ergodic random process. Explain what is meant by these characteristics.
5. Use the wind time history in the data file Wind\_vel.txt to compute the distribution of wind speeds 100 m above sea level using: a) all-year data; and b) seasonal data (winter (Dec–Feb); spring (Mar–May); summer (Jun–Aug); autumn (Sep–Nov)). Discuss the differences.
  - a. Plot the distribution of the mean wind speed on an all-year basis as well as a seasonal basis. Fit the distributions above to Weibull distributions. (You may assume  $\gamma = 0$ .)
  - b. Use the same data as above and compute the yearly as well as seasonal mean, median, maximum and standard deviation of the wind speed 100 m above sea level. Can you see any trends over the investigated period?
  - c. Choose four (or more) wind situations picked midday on a day in January, April, July and October. Investigate the wind profile by estimating the shear exponent\*. Discuss your findings.

\* = The shear exponent may be estimated using the wind velocity at two vertical levels. A better estimate is obtained using all levels you have data for. In the latter case you may take the logarithmic to the exponential relation and make a linear fit using a least-square fitting technique, i.e., you may do as follows:

Assume the mean velocities  $U_i$  are given at the vertical levels  $z_i$ . We want to find the exponent  $a$  that fits the exponential profile  $U(z) = U(z_r)\left(\frac{z}{z_r}\right)^a$ . Taking the logarithmic of this equation, we obtain a linear equation with two unknown quantities  $a$  and  $\log(U(z_r))$ :

$$\log(U(z)) = a \log\left(\frac{z}{z_r}\right) + \log(U(z_r)).$$

The two parameters can be found by fitting the equation in a least-square sense to the “observed” data. Use  $z_r = 10$  m. Instructions on how to fit data to a linear equation may be found here: <https://mathworld.wolfram.com/LeastSquaresFitting.html> (accessed July 2023; compare the above equation to equation 3 at the website).

6. Use the wind time history in Wind\_vel.txt and Wind\_dir.txt and sort the data with respect to wind direction. Use four direction intervals: 315 deg–45 deg



- (northerlies); 45 deg–135 deg (easterlies); 135 deg–225 deg (southerlies); and 225 deg–315 deg (westerlies).
- a. Compute the distribution of wind speeds 100 m above sea level for each direction. Are there any differences?
  - b. Can you explain the reason for the differences? (The data are from a site located far offshore in the North Sea (about 5°0' east, 56°5' north).
7. The file `WindTimeSeries.txt` gives a 40-min-long record of wind velocity at five vertical levels at a coastal site. The data are sampled at an interval of 1.1719 s. The file is organized in five columns, one for each height. The heights,  $z$ , in meters are given at the first line of the file. The wind speeds are given in m/s.
- a. Calculate the mean wind speed, standard deviation and turbulence intensities at the five heights.
  - b. Investigate how the observed mean wind profile compares to logarithmic and power law formulations.
  - c. Calculate the vertical coherence for the wind speeds using the 10 m level and the three levels above. Plot the coherences in a common plot and discuss the result.
8. Use the wave time history in `Wave_data.txt` to compute the distribution of significant wave height,  $H_s$ , using: a) all-year data; and b) seasonal data (winter (Dec–Feb); spring (Mar–May); summer (Jun–Aug); autumn (Sep–Nov).
- a. Discuss the differences. The data are from the same location as the wind data above.
  - b. Fit the distributions above to two-parameter Weibull distributions. (Use  $\gamma = 0$ .) Discuss the Weibull parameters found.
  - c. From the distributions of  $H_s$  above, find how large fraction of the time  $H_s$  is below certain limits (e.g., 1, 2 and 3 m) during the various seasons.
9. Make a 30-min time series of wave elevation by summation of a (large) number of regular wave components. Pick the amplitudes so that the time series represents a realistic wave spectrum. Use, for example,  $H_s = 5$  m,  $T_p = 10$  s and  $\gamma = 3.3$  in the Jonswap spectrum. Assume infinite water depth.
- a. Make a histogram of the wave heights in the time series and compare it to a Rayleigh distribution.
  - b. Repeat the generation of the time series and check how the maximum amplitudes compare with what should be expected from a Rayleigh distribution.

- c. Compute the wave elevation spectrum and check how it compare to the input you used.
- d. What does the horizontal velocity and acceleration time series look like at  $z = 0 \text{ m}$  and  $z = -10 \text{ m}$ ?
- e. Compute the spectra of the velocity and acceleration time series.
- f. Can you compute the spectra of the velocity and acceleration time series directly from the wave elevation spectrum?